

https://dspace.org/

SuperNec Method of Moments and Geometric Theory of Diffraction Hybrid Evaluation.

Rebuli, Craig Dino

2014-03-26
http://hdl.handle.net10539/14331

Downloaded from a DSpace repository. https://dspace.org/

SuperNec Method of Moments and Geometric Theory of Diffraction Hybrid Evaluation

Craig Dino Rebuli

A research report submitted to the Faculty of Engineering, University of the Witwatersrand, Johannesburg, in partial fulfillment of the requirements for the degree of Masters of Science in Engineering

Johannesburg, 1999

DECLARATION

I declare that this dissertation is my own unaided work. It is being submitted for the degree of Master of Science in Engineering in the University of the Witwatersrand, Johannesburg. It has not been submitted before for any degree or examination in any other University.

(Signature of candidate)

26 Day of JULY 19 99

Foreword

The Format for this Masters Dissertation consists of a short body (in the form of a technical paper) and multiple appendices. The technical paper is a valuable source of information as it encapsulates and summarises as much relevant material as possible in a paper sized document. The appendices contain the main substance of the project.

This document therefore differs from the standard dissertation format and is said to be of the 'Paper Model' format.

The project is called SuperNEC Method of Moments and Geometric Theory of Diffraction Hybrid Evaluation and deals with a new code used in the evaluation of electromagnetic structures. The new code is a hybrid of two well known methods namely Method of Moments (MOM) and Geometric theory of diffraction (GTD), and differs from other hybrids in that the hybridisation occurs at the interaction matrix instead of in the later stages of the calculations.

The Paper is titled "Evaluation of a MOM/GTD hybrid" and discusses the various methods used in evaluating the Hybrid code by comparing simulations to physical measurements and to theory. The focus of the paper being the approach to the simulations and results compared to the measurements, where possible, or compared to the results from a basic MOM structure.

The appendices give more detail on specific parts of the project, which are not detailed in the 'paper' section, and are as follows:

The literature survey in appendix A discusses the background theory that was required as an essential part of this project. The survey focused on the theory of MOM and GTD, as well as practical application of the two. A brief overview of measurement techniques is detailed along with the measurement procedure as a reference for future measurements.

Appendix B discusses the details of a previously measured 357MHz dipole. The reason for reproducing the measurements for this antenna is to test the accuracy of the results obtained in the anechoic chamber.

The 450 and 600MHz dipole in appendix C are used firstly to test the repeatability of measurements and then for the progression to the dipole and reflector plate test case in appendix D.

The dipole and reflector plate (Appendix D) describes the process involved in the simulations and measurements as well as graphically showing the results achieved.

Table of Contents

DECLARATION I

FOREWORD II

TABLE OF CONTENTS III

EVALUATION OF A MOM/GTD HYBRID 1

1 INTRODUCTION 1

1.1 BACKGROUND THEORY ON METHOD OF MOMENTS (MOM) 2
1.2 BACKGROUND THEORY ON UTD 2
1.3 BACKGROUND THEORY ON SUPERNEC 3

2 APPROACH 3

3 RESULTS 5

3.1 DIPOLE AND PLATE 5
3.2 DIPOLE AND PLATE HYBRID 7

4 CONCLUSIONS 8

5 REFERENCES 9

APPENDIX A : LITERATURE SURVEY .....

APPENDIX B : 357 MHZ DIPOLE .....

APPENDIX C : 450 AND 600MHZ DIPOLE .....

APPENDIX D : DIPOLE AND REFLECTOR PLATE .....

APPENDIX E : GTD/MOM HYBRID .....

Evaluation of a MOM/GTD Hybrid

C.D. Rebuli
Department of Electrical Engineering
University of Witwatersrand
Johannesburg, South Africa

Abstract: Super Numerical Electromagnetics Code (SuperNEC) is a MOM/UTD hybrid program with the MOM component based on the well known Numerical Electromagnetics Code (NEC) version 2. SuperNEC differs from other hybrids in that structures can be evaluated using either MOM or UTD, as well as combining both MOM and UTD in a hybrid at the interaction matrix level. Tests on a dipole and reflector plate using only MOM, then using a UTD plate and comparing the results to physical measurements are all in excellent agreement with differences of less than 5Ω (6%) for the real part of the impedance and 10Ω (12%) for the imaginary part. A Hybrid using both MOM and UTD on a single structure is also possible whereby large parts of the structure are constructed using UTD and smaller more detailed areas constructed using MOM. A hybrid reflector plate was tested and compared to the MOM reflector plate. The error was indirectly proportional to the size of the UTD plate, confirming that the UTD rule still holds, whereby for accurate results the UTD plate lengths must be larger than a wavelength in size. A hybrid structure has been shown to be possible as long as the part of the structure to be modelled using UTD is larger than a wavelength in size.

1 Introduction

The aim of this paper is to convey the results of tests and simulations run on a new Electromagnetic software program called SuperNEC.

SuperNEC is a hybridisation of the original Numerical Electromagnetic Code, NEC2, using Method of Moments (MOM) and Uniform Theory of Diffraction (UTD). Hybridising different methods is not a new development, as there have been other hybridised packages developed [Thiele 75]. What makes SuperNEC unique is that hybrid is achieved by introducing the UTD interaction into the MOM impedance matrix, as follows:-

$$[Zmn + Z^{utd}mn][In] = [Vm]$$

SuperNEC allows the user to combine NEC structures, made up of wires, and UTD, structures made up of plates or cylinders. Since NEC is known to give excellent results, I will show to what extent the hybridisation in SuperNEC compares with the results of pure NEC structures.

The reason for hybridising would be that whilst NEC gives excellent results for certain structures, it is not always the most practical to use. NEC segments each wire of a structure and then calculates the currents on each of these segments. This is extremely time consuming particularly for very large structures.

UTD uses ray theory and ray tracing techniques to calculate the amount of energy at certain points. In order to achieve accurate results the surfaces off which the rays are diffracted, and reflected must not be smaller than one wavelength. As UTD does not segment the structure, the time taken to calculate the relevant data is reduced from a NEC structure. This is only noticeable for larger structures and is dependent on the number of higher order terms included in the UTD simulation.

NEC is the most accurate but has constraints in processing time and power due to the number of segments involved in the calculation. UTD requires excitation of the structure by planar waves, which requires the structure to be larger than a wavelength. The more higher order terms included in the calculation the more accurate the results will be but the more processing time is required.
In other words NEC is excellent, both in accuracy and speed, for smaller structures, whereas UTD is better for larger structures where speed is desired.

As mentioned earlier the main purpose of this paper is to give details on the efficiency and accuracy of SuperNEC as compared to MOM. The approach to the problem has been to obtain a working model of a

basic structure, a dipole. The dipole was simulated using MOM and measured in an anechoic chamber. The dipole with an added reflector plate is used to include the UTD simulation. The plate and dipole assembly is simulated using MOM, where the plate is made up from a grid of wires, and then with a MOM/UTD hybrid where the dipole is a segmented wire (MOM) and the reflector is a solid plate (UTD). Once again the results from the pure MOM method are compared to the results from the hybrid as well as physical measurements.
MOM and UTD are also combined onto a into a single structures, and is achieved by taking the same sized reflector plate as before, and making the plate part grid and part solid plate thereby combining the MOM and UTD methods together on a single structure.

The details of the project are laid out in this paper by firstly giving some background theory on MOM, UTD and SuperNEC, followed by details on each of the structures and the measurement and simulation procedure. Results are given showing the relevant radiation patterns. Impedance plots are given for the simple dipole to show the accuracy of the simulation to the measurements as the impedance is difficult to obtain accurately. Radiation patterns are given for the other structures as the impedance is simply a matching problem whereas the radiation pattern is more useful in that an overall characteristic of the antenna is shown. The impedance of a structure is also calculated, in MOM, based on the size of the segment, whereas the radiation pattern takes into account more than only the current from one segment.

1.1 Background Theory on Method of Moments (MOM)

MOM calculates the [E]-field at a distance from the structure by firstly segmenting all linear wires of the structure [Burke 81]. Assuming that the wire radius is small, current will flow axially along the structure, as shown in figure 1.1.

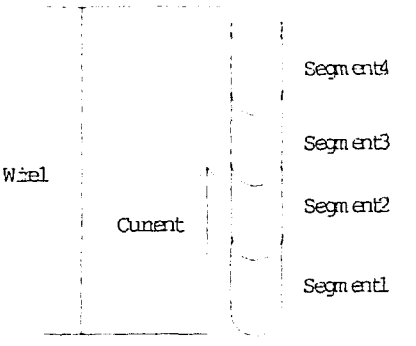


Figure 1.1: MOM wire model

Maxwell's equation is used to develop a relationship between E tangential and the current on the wire. The developed expression is known as Pocklintons equation. The unknown current distribution can then be found from the E-field, which is known since this is the field used to excite the structure.

The current is approximated for each segment of the wire using a basis function. By vectorially adding all the current contributions, a complete approximation to the current on the wire is established. The number of segments will determine the accuracy of the approximation. Increasing the number of segments increases the accuracy, but may also produce segments that are short relative to the radius, invalidating the assumption that the current flows axially along the wire.

The current distribution can be calculated from the following matrix:-

$$[Z][I]=[V]$$

Where Z may be calculated from the geometry of the problem and V is determined by the method of exciting the structure [E].

Once the current has been found based on the excitation voltage, other parameters such as the impedance, near fields and far fields, can then be calculated.

1.2 Background Theory on UTD

One of the most versatile and useful high frequency techniques is the UTD, which was developed around 1951 by J.B. Keller [Lo 93]. UTD is based on modern physics, where rays are reflected and diffracted from surfaces and edges. The trajectories

of a ray can be computed using the law of reflection or Snells law of refraction.
Components of the diffracted fields are found using the individual rays, which are summed with the geometrical optics terms in the far field. The rays from a given scatter tend to interact with other structures causing various higher order terms. In this way one can trace out the various possible combinations of rays using only the dominant terms or including higher order for a more accurate analysis. Complex problems can be built up from simpler problems in manageable pieces [Markefka 79]. As a result, the GTD provides an efficient high frequency solution to problems that are difficult to solve using MOM. For example, an analysis of complex radiating systems such as antennas on aircraft, missiles, or ships can be performed efficiently by simulating those structures with appropriate models, which are built from simpler shapes. These simpler shapes carefully simulate parts of the actual structure that dominate the reflection and diffraction effects.
The ability of the GTD to accurately solve the problems of electromagnetic radiation and scattering from complex structures, in a relatively simple and efficient manner makes it a very powerful tool for antenna design. For example, an analysis of complex radiating systems such as antennas on aircraft, missiles, or ships can be performed efficiently by simulating those structures with appropriate models, which are built from simpler shapes, like plates and cylinders.

1.3 Background Theory on SuperNEC

SuperNEC is an object-oriented version of the FORTRAN program NEC2, with the added advantage of hybridising MOM and UTD. SuperNEC will allow the user to incorporate both MOM and UTD structures into a simulation involving large and small structures. Most other hybrids do not change the interaction matrix, but do a far-field pattern approximation. The UTD can be combined with the MOM solution by treating the UTD field as a scattered field and modifying the interaction matrix, Z, as follows:-

$$[Zmn + Z^{utd}mn][In]=[Vm]$$

Here, $Z^{utd}mn$, is the impedance matrix modification associated with the radiation from current elements in In scattered by the UTD structure in terms of the UTD mechanism and reacting with the observation current Im.

UTD structures implemented include plates and cylinders [Nitch 98]. The disadvantage of UTD is that structures should be larger than a wavelength for accurate results, whereas the disadvantages of NEC are the time and memory constraints occurring with larger structures. Hybridising NEC and UTD reduce these limitations.

2 Approach

The approach was to obtain a working dipole to use as a reference. The dipole is simulated using MOM and compared to measurements taken on a physical dipole in an anechoic chamber. A reflector plate, made from a grid, is added to the MOM simulation, which is compared to the dipole with a UTD reflector plate. Measurements of the dipole and reflector plate in the anechoic chamber are then compared to both the MOM and UTD simulations. Finally a hybrid is produced, using both MOM and UTD, on the reflector plate. The results are compared to the simulated results from the pure MOM reflector plate or grid.

The dipole, shown in figure 2.1, has been constructed from 1.6mm brazing rod, and is fed via RG400 coaxial cable. A sleeve or 'Bazooka' balun is used to reduce unwanted currents flowing down the coaxial cable. A wooden beam 25mm square has been used to support the dipole and cable. The beam allows for the cable to be taken from the centre of the dipole, straight back as far as possible to reduce reflections, which may interfere with the measurements. The dipole has been extended over the edge of the beam, and held in place with cardboard and masking tape, also to reduce interference from the beam.

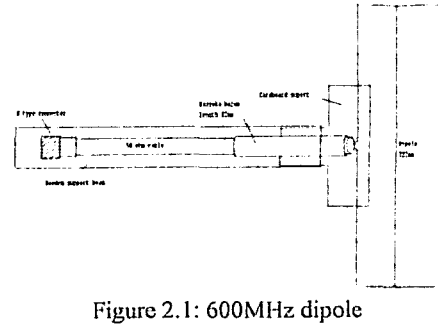


Figure 2.1: 600MHz dipole

The dipole is then placed on a wooden stand in the quiet zone of the anechoic chamber, as shown in figure 2.2. The quiet zone was found by moving the dipole to various positions in the chamber and measuring the variation in the measurements. The coaxial cable is then taken through a special connecting plate, in the wall of the anechoic chamber, to the Network analyser on the outside of the chamber. The network analyser allows for the coaxial cable to be calibrated out of the equation, so that effectively, direct measurements at the feed point of the dipole may be taken.

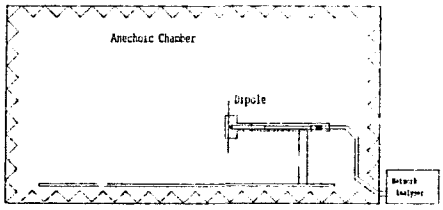


Figure 2.2: Impedance measurements in the chamber

The results of the impedance measurements of the dipole are shown in figures 2.3 and 2.4. Figure 2.3 shows the real impedance while figure 2.4 shows the imaginary impedance. Figures 2.3 and 2.4 shows a maximum error of 7% between the simulated dipole, using MOM, and the actual measurements on the dipole. The results also confirms results by Dresel on dipole measurements [Dressel 96]. The range over which the comparisons are valid is determined by the balun, which has an approximate bandwidth of 10%, between 600MHz and 660MHz. Outside of this band the error becomes too great to work with. The reason for the 10% bandwidth of the balun is that the balun is a ¼ electrical wavelength long, which means that it is frequency dependant, and has only a small bandwidth over which it works [Kraus 88 Jasik 61].

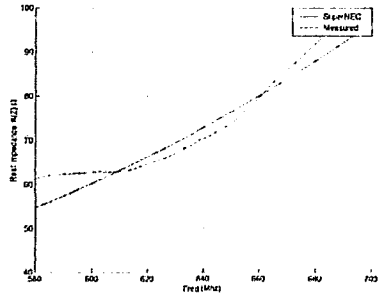


Figure 2.3: Real impedance of the 600MHz dipole

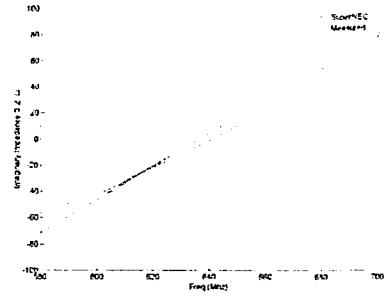


Figure 2.4: Imaginary impedance of the 600MHz dipole

Having achieved a good comparison between simulated and measured results for a simple dipole, a structure was considered which can be simulated using both MOM and UTD. As UTD can be modelled using plates and cylinders, a reflector plate behind the dipole was used. The dipole used is the same dipole as above, as the results have been proved to be accurate. The reflector plate has been made one wavelength by one wavelength in size. Modelling was done first using MOM, where the plate has been constructed from a grid of wires, based on the equal area rule for modelling plates [Trueman 90, Ludwig 87, Mayhan 90]. The plate was converted to a solid plate to be simulated using UTD. Finally a dipole and reflector plate was built for physical measurements. An aluminium sheet was used for the plate due to it being lightweight as well as having good conductance. (Aluminium = 3.5×10^7, steel = 1×10^6). A square hole was cut into the plate to allow for the wooden support boom and cable to pass through, ensuring that the plate has a firm stable support as well as to keep the cable away from areas which may cause interference, see fig 2.5. The measurements of the dipole and reflector plate took place in the anechoic chamber, starting with impedance measurements as described above, followed by radiation pattern measurements.

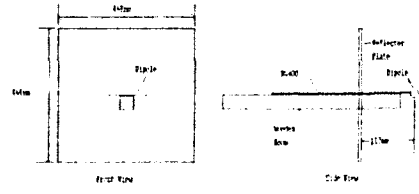


Figure 2.5: Dipole and plate construction

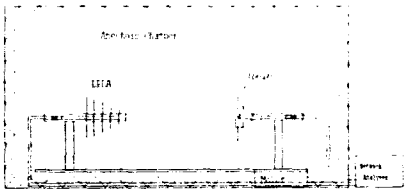


Figure 2.6: radiation pattern measurements in the chamber

The radiation pattern measurements required the use of a high gain antenna, a Log Periodic Dipole Array (LPDA) [Evans 90, Burberry 92], to transmit a signal, which is received by the dipole and reflector plate under test (see fig 2.6). The received signal is then fed to a network analyser which then stores the data in a form suitable for analysis of the radiation pattern. The results for these tests are shown later.

Finally a combination of MOM and UTD were used to model the reflector plate to determine whether a MOM and UTD hybrid can be created on a single structure, while still giving fairly accurate results. One of the reasons you may want to do this is if you have a large structure, such as an aircraft. Certain parts may need to constructed from a grid, for more detail and other parts, such as the wings, have less detail and can be constructed from plates.

The reflector plate is a good structure on which to attempt this, arbitrarily starting by making the inside half a solid plate and the outside a MOM grid, as shown in figure 2.7, followed by the inverse, consisting of the MOM grid in the centre and a UTD plate, or plates as four separate plates were required, on the outside, as in figure 2.8. The third model, in figure 2.9, is a modification of the first one with the plate on the inside and the MOM grid on the outside, with the difference being that the plate has been made to cover a larger area, 90% of the total plate size. Once again these simulations are compared to the pure MOM plate and dipole simulation, as the MOM simulation is known to be correct. The results are given in the next section.

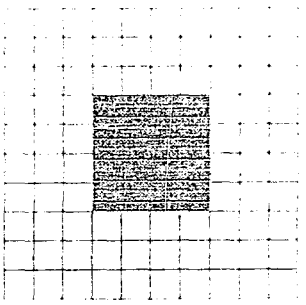


Figure 2.7: GTD plate inside and MOM grid on the outer area.

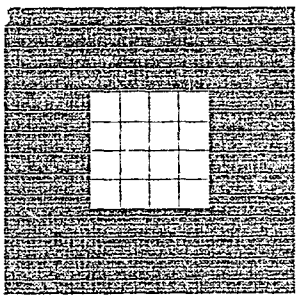


Figure 2.8: MOM grid in the middle with GTD plates on the outer area.

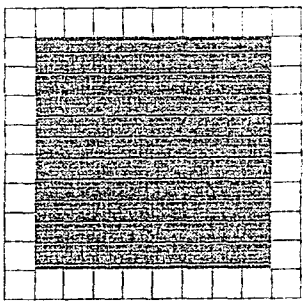


Figure 2.9: Larger GTD plate inside with a smaller MOM grid on the outer edge.

3 Results

3.1 Dipole and plate

The measured and simulated impedance for the dipole and plate are shown in figure 3.1 and 3.2 below. Figure 3.1 shows the real part of the impedance while figure 3.1 shows the imaginary part of the impedance. The error when comparing the

UTD to the MOM model is at most 1Ω (an error of 1.25%) for both the real and imaginary plots. The error when comparing measured data to the MOM simulation is as good as the data for the simple dipole, shown previously. The error is less than 5Ω (an error of 6%) for the real impedance and less than 10Ω (an error 12.5%) of for the imaginary impedance. The reason for the larger error is because of the interactions between the cable and the reflector plate as well as reflections in the chamber. The impedance for the dipole and plate has also increased by about 20Ω from the simple dipole simulation due to the inclusion of the reflector plate [Kraus 88].

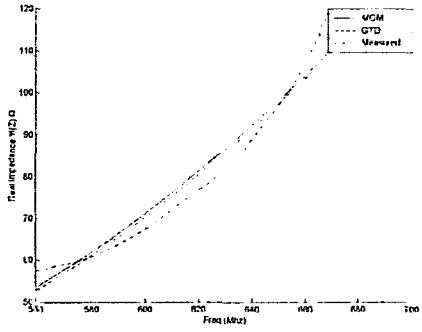


Figure 3.1: Real impedance of the dipole and plate.

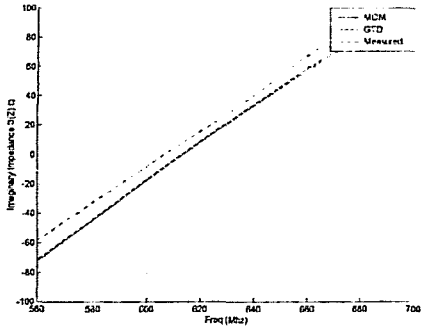


Figure 3.2 : Imaginary impedance of the dipole and plate.

The radiation pattern simulations of MOM and UTD, shown in figure 3.3 and 3.4, are virtually indistinguishable and compare well to results detailed in Kraus and the NEC2 Manual [Kraus 88, Burke 81]. The largest error appears at the nulls, 0 and 180°, and is caused by a mathematical discrepancy produced in the program itself. The measured radiation pattern compares very well to the simulated models, with the greatest accuracy occurring in the higher gain areas in front of the antenna, better than 2%. The less accurate portion of the radiation pattern occurs in the back radiated section where the gain is less than unity, the difference being 2dBi between the MOM and measured values, translating to an error of 20%. The larger errors occur due to the fact that the network analyser has difficulty distinguishing between the low signal and the surrounding noise levels. The LPDA can be moved closer to the dipole and plate to increase the signal amplitude received by the network analyser, but then the R=2D/λ rule is violated [Rudge 82]. Where D is the diameter of the test antenna and R is the distance between antennas. The other reasons for the errors in the measurements are because of the reflections that occur from the walls of the chamber. The interfering reflections can be reduced by changing the position of the antennas in the chamber, but do not change the pattern much as the antennas are in the quiet zone of the chamber.

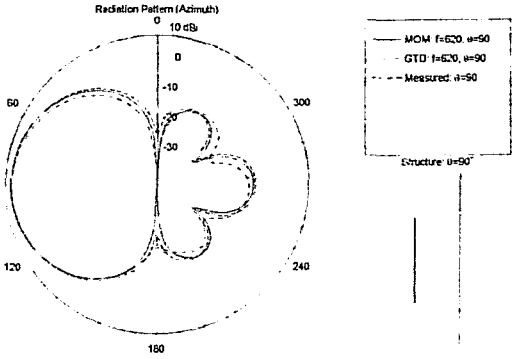


Figure 3.3: Azimuth patterns for the dipole and plate.

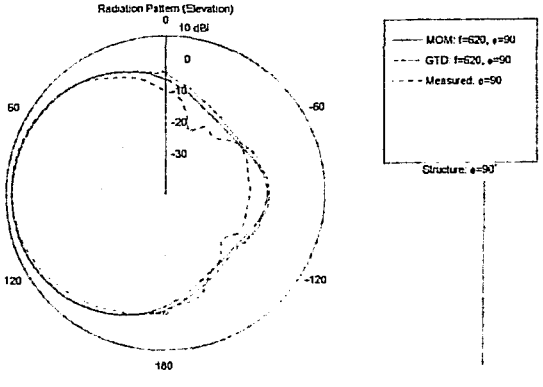


Figure 3.4: Elevation pattern for the dipole and plate.

3.2 Dipole and Plate Hybrid

Since the measured results compare favourably with the MOM implementation in the previous section, all hybrid results in this section are compared to the MOM results as a reference.

A hybridisation of MOM and UTD has been attempted, starting with half the reflector plate made from a grid and the other half from a UTD plate. The UTD plate is in the centre and the MOM grid on the outer edge. Figure 3.5 and 3.6 show the results of the radiation pattern for the hybrid, compared to the pure MOM plate. The radiation patterns compare extremely well in the forward direction, between 60 and 120°, but nowhere else. The nulls, at 0°, 180°, 240° and 300° are not indicated at all. There is more back radiation on the hybrid, 10dBi more than the MOM simulation. No improvement was achieved by turning on or off the various diffraction and reflection terms.

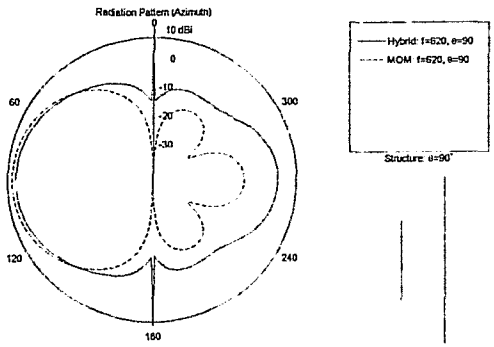


Figure 3.5: Azimuth pattern for the hybrid with the small UTD plate in the centre

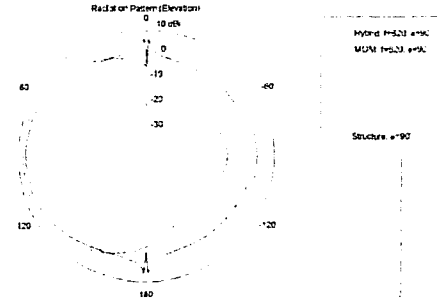


Figure 3.6: Elevation pattern for the hybrid with the small UTD plate in the centre

As UTD requires large surfaces from which to work [McNamara 90], the plate hybrid has been inverted, with the UTD plate being on the outer edges and the MOM grid in the centre. The results in figures 3.7 and 3.8, showing the azimuth and elevation radiation patterns, are better than the previous hybrid. The most accurate comparison is still in the forward radiation, between 60 and 120°. The nulls at 0 and 180°, which were not indicated at all on the previous hybrid, are showing a close comparison to the MOM simulation. The back radiation is however still very much larger than that shown by the MOM simulation. Once again no improvement has been achieved by turning on or off the various diffraction and reflection terms.

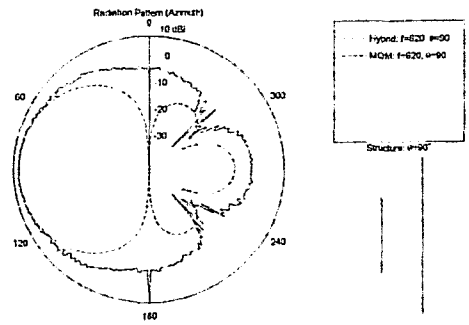


Figure 3.7: Azimuth pattern for the hybrid with the MOM grid in the centre.

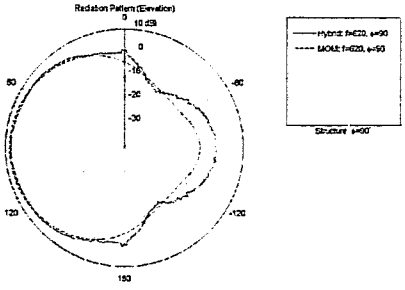


Figure 3.8: Elevation pattern for the hybrid with the MOM grid in the centre.

As this model gave a closer approximation to the MOM results, due to the increased size plate, another simulation was performed using a 0.8λ by 0.8λ plate, with the MOM area being smaller, then rerunning the simulation. Figure 3.9 shows the azimuth pattern and figure 3.10 shows the elevation pattern. The results of this hybrid when compared to the MOM model are even more accurate than the previous two hybrids. The most accurate comparison is still in the forward direction from 0 to 180°, with the least accurate being in the back radiated area. All the nulls are indicated at the correct positions, even though there is still a discrepancy in the gain at certain points. The back radiation at 270° is virtually the same as the MOM model, with an accuracy of less than 1dBi. Obviously by making the plate larger has increased the accuracy when compared to the pure MOM plate. The results indicate that the usual UTD rules still hold, whereby the sides of the structure must be larger than a wavelength for accurate results.

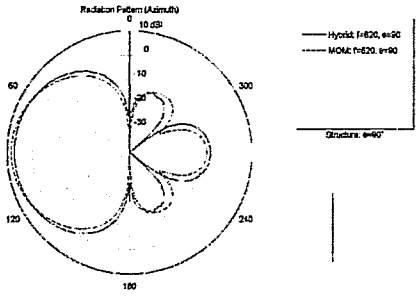


Figure 3.9: Azimuth pattern for the hybrid with the 0.8λ UTD plate in the centre

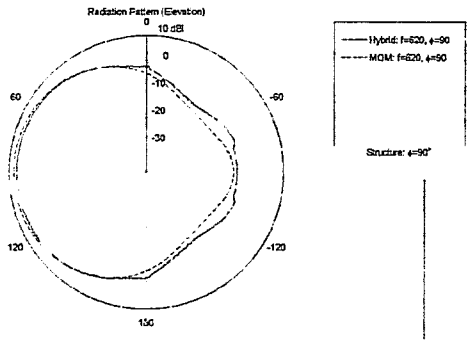


Figure 3.10: Elevation pattern for the hybrid with the 0.8λ UTD plate in the centre

A final Hybrid was run with a 2λ by 2λ reflector plate with firstly a UTD plate 50% (1λ by 1λ) of the 2λ area, followed by a larger plate taking up 80% of the 2λ area. Figure 3.11 shows the azimuth pattern and figure 3.12 shows the elevation pattern. As in the previous hybrid with the 0.8λ plate the most accurate results are in the forward direction with the least accurate results occurring in the back radiated section. The accuracy of the results when compared to a MOM model increase as the plates size increases. Confirming firstly that the UTD rule must be adhered to for results comparable to the MOM model and that the UTD plate must make up a large percentage of the reflector plate area to increase the accuracy in the back radiated region.

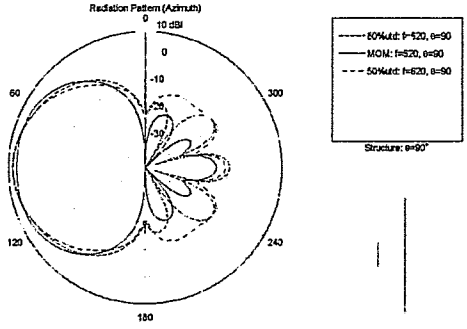


Figure 3.11: Azimuth pattern for the 2λ hybrid with the 1λ (50%) and 1.6λ (80%) UTD plate in the centre

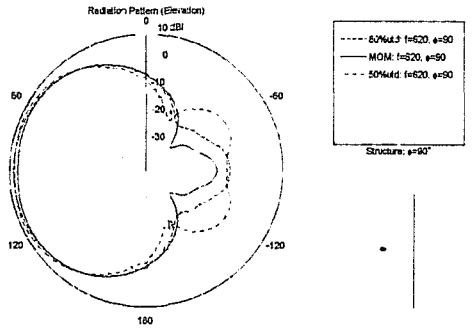


Figure 3.12: Elevation pattern for the 2λ hybrid with the 1λ (50%) and 1.6λ (80%) UTD plate in the centre

Only radiation patterns have been shown for these results, as they tend to give more information about the antenna than the impedance plots.
Even though the impedance plots are not exactly comparable, the radiation patterns appear to be far more accurate. The reason for this is that while the impedance is found for one segment on the structure, the radiation pattern is found from the interaction between all the segments.

4 Conclusions

This project has progressed from a basic dipole which has been simulated and measured, to a dipole and hybrid reflector plate simulated using both MOM and UTD.

The dipole was used to achieve a basis model from which further investigation was done and gave an excellent comparison between the simulated and measured values. As the dipole is known to be correct, a λ by λ (462mm by 468mm) reflector plate has been added to gain a comparison between MOM and UTD. Once again the results compare extremely well with an error of less than 1Ω for the real and imaginary impedance. The measured results do not give as close a comparison as the simulated, with the error being less than 5Ω for the real impedance and 10Ω for the imaginary impedance. These errors are due to measurement problems, associated with reflections in the chamber as well as mismatches with the balun. The radiation patterns of the MOM and UTD simulation are comparable with the gain difference being less than 1dBi between them. The measured radiation pattern is also comparable with a maximum error of less than 5dBi in the back radiated direction, which may be mostly to do with reflections in the chamber and partly because the network analyser loses the signal in the noise levels.

Four hybrids have been attempted, whereby part of the reflector plate is made from a UTD plate and rest of the plate is made from a MOM grid. The grid wires are joined to the UTD plate, producing a hybrid of MOM and UTD on the same structure. The first structure with the small (0.5λ by 0.5λ) UTD plate in the in the middle, and the MOM grid on the outer edge gives the worst results. The next hybrid is the inverse, with the grid in the centre and the plate on the outer edges, gives slightly better results, but still not in any useably form. The third hybrid is similar to the first except that the plate has been increased from $0.5\lambda^2$ to $0.8\lambda^2$ and the grid reduced to fill the remaining $1\lambda^2$ area. The final hybrid, completed to confirm the conclusion made from the previous hybrid, consists of a $1\lambda^2$ plate, and a 1.6λ plate, inside a grid extended to $2\lambda^2$. The results for the final two hybrids give a closer comparison to the non- hybridised MOM or UTD model. Proving that the plate must be at least one wavelength in size for results comparable to a pure MOM plate and should be a large percentage of the overall plate size for increased accuracy in the back radiated section.

The results when comparing the UTD simulations to the pure MOM structures are in excellent agreement, confirming that the SuperNEC hybrid works as well as pure MOM. i.e. with the dipole constructed from segments and the reflector plate constructed from either a grid or a UTD plate. Hybridisation of MOM and UTD on a single structure is also possible, provided that the UTD structure is equal to or larger than a wavelength. This allows for large structures which require detail in certain areas to be modelled using MOM and the less detailed areas to be modelled using UTD.

Work on SuperNEC is continuing, as there are still a few problems to be rectified, such as the mathematical discrepancies at certain angles in the radiation patterns. More tests using various structures need to be carried out to determine the limitations of the SuperNEC hybrid.

5 References

Burke G J, Pogio A J. *Numerical Electromagnetic code (NEC) - Method of Moments* 1981.

Burberry R A. *VHF and UHF Antennas* 1992.

Dressel J, Fourie A P C, Givati O, Clark A R. *The modelling of lossy surfaces using a Wire Method of Moments Code.* Symposium on Antenna Technology and Applied Electromagnetics, 1996 Conference Proceedings, Aug 6-9.

Evans G E. *Antenna Measuremnt techniques* 1990.

Jasik H. *Antenna Engineering Handbook* 1961

Kraus J D. *Antennas - second edition* 1988.

LO Y T, Lee S W. *Antenna Handbook Vol1* 1993.

Ludwig A C. *Wire Grid modelling of Surfaces* IEEE Transctions on Antennas and propagation, Vol AP-35, No 9 September 1987.

McNamara D A. Pistorius C W I,

Malherbe J A G. *Introduction to the geometrical theory of diffraction* 1990.

Marhefka R J, Burnside W D. *Numerical Electromagnetic code(NEC) Basic Scattering code part 1: Users Manual* 1979.

Mayhan J T. *Characteristic Modes and wire grid Modelling* IEEE Transactions on Antenna and Propagation Vol 38 No 4 April 1990.

Nitch D. *MOM-GTD Hybrid Reference Manual* 1998.

Rudge A W, Milne K, Olver A D, Knight P. *The handbook of Antenna Design* Vol 1 1982.

Thiele G A, Newhouse T H. *A Hybrid Technique for Combining Moment Methods with the Geometric Theory of Diffraction* IEEE Transactions of Antennas and Propagation Vol AP-23, Jan 1975.

Trueman C W, Kubina S J. *Verifying Wire Grid Modelling integrity with program check* ACES Journal Vol 5 No 2 1990.

Appendix A : Literature Survey

1 Theory on MOM and GTD

Both GTD and MOM have limitations with GTD sometimes failing when the radius of curvature is too small in wavelengths or when edges are too close together in wavelengths. Method of moments is limited by large or complex structures requiring many segments, hence many simultaneous equations. For some types of problems these two powerful techniques can be combined to yield an effective result which neither could do alone [McNamara 90, Thiele 75]. The following sections give an overview of MOM and GTD but for more detailed analysis the references can be consulted.

1.1 MOM

The fundamental theory-underlying MOM may be explained by considering a linear wire of radius a, as shown in Figure 1[Fourie 91].

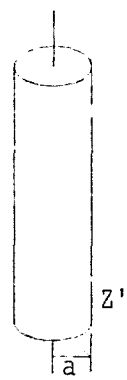


Figure 1: Cylindrical conductor of radius a

If the conductivity σ=infinity the total current can be considered to flow on the surface and the current at point z' on the conductor surface would be:-

$$I(z')=K(z')2\pi a \qquad (1.1)$$

Where K(z') is the surface current density at Z'. The total current is hence at a distance a from the z-axis, and we will consider it as flowing in empty space along an infinitesimally thin filament parallel to the z axis as shown in figure 2 below.

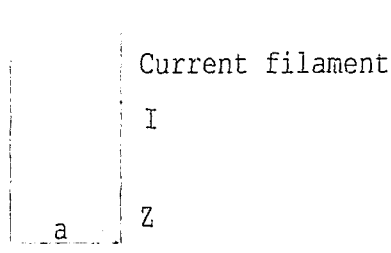


Figure 2: Conductor replaced by current filament

Note: There are a number of assumptions inherent in this defined scenario:

- Current on a specific wire is considered to flow in the axial direction only. This condition will hold only if $a<<\lambda$, the free space wavelength.
- Wires must have high conductivity for this theory to apply. Wires with finite conductivity may be analysed using MOM theory as long as the skin depth,δ, is small in comparison with a.

Maxwell's equation may now be used to develop an expression for the scattered E-field on a wire segment of length L. The starting point of such a derivation is illustrated in figure 3 below which shows how the E-field can be found by considering first an elemental part of the current at Z' (source point) and its resulting E-field at some observation point z.

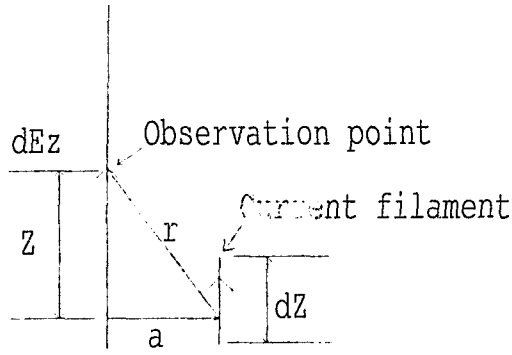


Figure 3: Source point on current filament

The mathematics can be solved with the final expression being the well-known Pocklintons equation:

$$E_z = \frac{1}{4\pi j\omega\varepsilon}\int_{-l/2}^{l/2}\left(\frac{\partial^2}{\partial_z^2}G_{zz'} + \beta^2 G_{zz'}\right)I(Z')\partial_{z'} \qquad (1.2)$$

Where

$G_{zz''} = \frac{e^{-j\beta r}}{r}$ = Free space Green's function

And

$$r = \sqrt{(z - z')^2 + a^2}$$

Pocklintons equation hence provides an expression giving the so called radiated field, Ez in terms of the current distribution I(z') on a wire. The current on the wire must be caused by some incident E field, E(z), which may either be due to a source applied tot he wire or an incident EM wave on the wire.

Note: In MOM analysis the unknown is the current distribution, I(z) on the wire whereas the source field E(z) is known since this is the field we use to excite the structure (either a voltage source for a transmitting antenna or a incident E-field for a receiving antenna. The unknown is hence under the integral sign and the MOM is the technique for efficiently solving such a problem by applying suitable boundary conditions.

The obvious boundary condition is provided by the fact that the total tangential E field on the conductor boundary must be zero since the conductivity of the wire was assumed to be large. Hence

$$Ez(\text{incident}) = -Ez(\text{scattered}) \qquad (1.3)$$

Development of a linear set of equations and matrix solution

The problem is approached by breaking the wire into N segments, each $\Delta z'_n$ in length. The observation point may then be considered to be on a segment m and the source point on a general segment n.

Equation 1.2 can then be rewritten in the following notation:

$$-E(z') = \int_{-l/2}^{l/2} I(z')G(r_{mn})dz' \qquad (1.4)$$

Where:
$r=r_{mn}$
m= observation point (z)
n=source point (z')

$$G(r_{mn}) = \frac{1}{4\pi j\omega\varepsilon_0}\left(\frac{\partial^2}{\partial z^2}Gzz' + \beta^2 Gzz'\right)$$

The current is approximated by a series of so called expansion functions in order to develop a set of equations to solve the problem:

$$I(z') = \sum_{n=1}^{N} I_n F_n(z') \tag{1.5}$$

The expansion function $F_n(z')$ is normally chosen to be a function valid over segment n of the wire while being zero elsewhere. By adding all the current contributions as indicated by equation 1.5, a complete approximation to the current on the wire is established. The most obvious choice of function to use is the pulse function (unity on segment n and zero elsewhere). The coefficient I_n will then determine the magnitude of the current pulse on each segment and typical current approximation such as illustrated in figure 4 may be found.

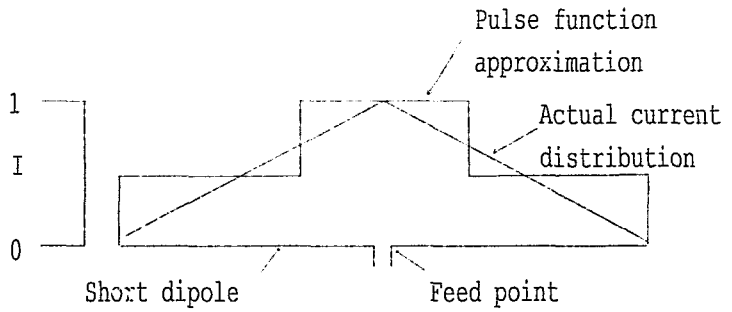


Figure 4: Step (pulse function) approximation and actual (triangular) current distribution on a short centre fed dipole antenna.

Note: The accuracy of the final solution is clearly dependent on the number of segments the wire is divided into with more segments increasing the accuracy of the approximation. Increasing the number of segments, however, may result in segment lengths, which are short relative to their radius, which invalidates the assumption of axial currents stated earlier.
After segmentation and choosing an expansion function the problem hence reduces to that of obtaining a solution to the unknown coefficients, I_n. Considering the mth segment and using 1.4 and 1.5 we have

$$-Ez'(z_m) = \sum_{n=1}^{N} I_n \int_{\Delta z'_n} G(r_{mn})\,dz' \tag{1.6}$$

And

$$G_{mn} = \int_{\Delta z'_n} G(r_{mn})\,dz' \approx G(r_{mn})\Delta z'_n \tag{1.7}$$

And writing out 1.6 in full gives an equation for the mth segment

$$-Ez(Z_{..}) = I_1 G_{m1} + I_2 G_{m2} + \ldots + I_N GmN \qquad (1.8)$$

This is one equation with N unknowns obtained by enforcing the boundary condition at segment m. A solution to the values of the current coefficients I_n may be obtained by enforcing the boundary conditions on segments m=1...N which yields the following equations.

Note: Enforcing the boundary condition at each segment implies that the condition of zero tangential field is exact at the chosen match points (normally the centre of each segment) and may well be violated at points in between. Segments must hence be chosen small enough such that this residual error is kept to a minimum.

$$\begin{array}{lllll}
I_1G_{11} & + & I_2G_{12} + \ldots & +I_NG_{1N} & = -E_{z'}(Z_1) \\
I_1G_{21} & + & I_2G_{22} + \ldots & +I_NG_{2N} & = -E_{z'}(Z_2) \\
\vdots & & \vdots & & \\
\vdots & & \vdots & & \\
\vdots & & \vdots & & \\
I_1G_{N1} & + & I_2G_{N2} + \ldots & +I_NG_{NN} & = -E_{z'}(Z_N)
\end{array}$$

Which can be shown in a matrix format as

$$\begin{bmatrix} G_{11} & G_{12} & \ldots & G_{1N} \\ G_{21} & G_{22} & \ldots & G_{2N} \\ \vdots & \vdots & \vdots & \vdots \\ \vdots & \vdots & \vdots & \vdots \\ \vdots & \vdots & \vdots & \vdots \\ G_{N1} & G_{N2} & \ldots & G_{NN} \end{bmatrix} X \begin{bmatrix} I_1 \\ I_2 \\ \vdots \\ \vdots \\ \vdots \\ I_N \end{bmatrix} = \begin{bmatrix} -E_{Z'}(Z_1) \\ -E_{Z'}(Z_2) \\ \vdots \\ \vdots \\ \vdots \\ -E_{Z'}(Z_N) \end{bmatrix}$$

This matrix in the compact form is:

$$[Z]\bullet[I]=[V] \qquad (1.9)$$

This is solved by:

$$[I]=[Z]^{-1}\bullet[V] \qquad (1.10)$$

Note:

- A N segment problem results in a N X N matrix
- The values for the Z, or interaction matrix may be calculated from the geometry of the problem. In essence the Z values describe the interaction between general segments m and n of the structure. The similarity to a set of network equations should be apparent.
- The value of the V, or excitation matrix is dependent on the method of excitation of the structure. The excitation specified is translated into an excitation per segment i.e. a transmitting antenna will have a zero E-vector except for the E-vector value corresponding tot he driven segment (Feed point) of that antenna. When modelling a structure a segment must be defined at the position where the user intends to apply a source.

Currents, near field, far fields, coupling and impedance

Currents

Solving 1.9 gives the current coefficients for each segments' current function. This is equivalent to the actual current value since pulse functions were chosen resulting in a staircase approximation to the actual current (Fig 4). Once the current on a structure due to a specific excitation is known all other electromagnetic characteristics may be determined from fundamental theory.

Near Fields

Each segment of wire in the structure is equivalent to an ideal dipole since it is small in terms of wavelength and has a constant current, if pulse expansion functions were used. Those may hence approximate expressions for the near fields from such a segment from an ideal dipole. For a segment of length, L with current I these are as follows:

$$E_r = \frac{IL\cos\theta}{2\pi\varepsilon_o}\left(\frac{\cos\omega t'}{r^2 c} + \frac{\sin\omega t'}{r^3\omega}\right) \tag{1.11}$$

$$E_\theta = \frac{IL\sin\theta}{4\pi\varepsilon_o}\left(\frac{-\omega\sin\omega t'}{r\ c^2} + \frac{\cos\omega t'}{r^2 c} + \frac{\sin\omega t'}{r^3\omega}\right) \tag{1.12}$$

$$H_\phi = \frac{IL\sin\theta}{4\pi}\left(\frac{-\omega\sin\omega t'}{rc} + \frac{\cos\omega t'}{r^3}\right) \tag{1.13}$$

Where

E_θ, E_r and H_ϕ are the near E and H fields in the directions as indicated by the subscripts and
ω is the radian frequency ($2\pi f$)
r is the radial distance from the segment
c is the speed of light
ε_o is the permittivity of free space
θ is the angle with respect to the segment axis
$t'=t-r/c$ which provides phase information.

Equations 1.11-1.13 may be used to calculate the field contribution at a specific point due to one segment given the current on the segment and its length. The total near fields may then be obtained by vectorially adding all the contributions from the structure.

$$E_{rTotal} = \sum_{n=1}^{N} E_{rn} \qquad (1.14)$$

Where E_{rn} is given by expression 1.11 applied to segment n. The other field contributions are found in a similar fashion.
Note: The calculations of the near fields hence involve contributions due to currents on all segments of the structure simulated. These calculations hence tend to be more accurate than those involving only localised currents on the structure such as input impedance, efficiency and coupling which will be discussed later.

Far Fields

The far fields, which determine the structure, directionally characteristics may be found from the currents on the structure in a similar way. Assuming once again that a segment radiates like an ideal dipole the E field due to a single segment is given by:

$$E_\theta = \frac{60\pi I}{r}(L/\lambda)\sin\theta j e^{j\beta r} \qquad (1.15)$$

Where $\beta = 2\pi/\lambda$

The far H-field due to the same segment is given by:

$$H_\phi = \frac{E_\theta}{120\pi} \qquad (1.16)$$

And the power density, P_d by:

$$P_d = E\theta x H\phi \tag{1.17}$$

The total field from a structure comprising of many segments is once again found by vectorially adding the contributions to individual segments.

Antenna gain is obtained by comparing the power density in a specific direction to that of the power the power density which an isotropic source with the same input power as the actual structure would produce.
Note: The relative radiation pattern of a structure is hence also a quantity obtained by considering all the segments and is, for this reason, quite accurate. The absolute gain of the antenna however uses both radiated power quantities as well as antenna input power and the input power is dependent on local currents at the antenna input, which may be less accurately calculated. Errors in the input power calculations manifest themselves in a constant (dB) error in the absolute gain figures while the pattern shape is more accurate

Input impedance, efficiency and coupling

The antenna input impedance, if segment m contains a source voltage, v, is determined by using the current, I_m on that segment.

$$Z_{in} = \frac{V}{I_m} \tag{1.18}$$

Note: Input impedance is a function of the current on one segment of a structure. Even if the general current distribution on a structure is quite accurately determined the input impedance may be in error by a large amount if the current on the input segment is not correct. The voltage V specified by the user is also converted by the package into an E field excitation at that segment. Other fields due to radiation altering it may alter the segment E field however. This is not taken into account and may results in additional errors in calculating the input impedance.
The antenna radiation efficiency, η, is calculated by:

$$\eta = \frac{P_{in}}{P_{in} - P_{loss}} \tag{1.19}$$

Where

$$P_{in} = |I_m|^2 R(Z_{in})$$

And

$$P_{loss} = \sum_{i=1}^{M} |I_i|^2 R(Z'_i)$$

With Z'_i the i-th load (i=1...k) on a structure and I_i the current on the i-th load.
Antenna coupling may be calculated by the Linvilee method to yield to maximum coupling, G_{max} between two ports on a structure.

The two port admittance parameters are computed in NEC2 by exciting each antenna with the other short circuited and computing the self and mutual admittances.

$$G_{max} = \frac{1}{L}\left(1 - \sqrt{1 - L^2}\right)$$

Where

$$L = \frac{|Y_{12}Y_{21}|}{2\,\mathrm{Re}(Y_{11})\mathrm{Re}(Y_{22}) - \mathrm{Re}(Y_{12}Y_{21})}$$

Note: Max coupling assumes that the antennas are perfectly conjugate-matched to their sources and receiver impedances. The real effect or noise power which will result, due to such coupling must hence first account for the additional mismatch losses which normally reduces the coupling if the antennas are not operating at exactly the same frequency.

Computer time and memory requirements

The computer time is mainly a function of the time taken to fill and factor the interaction or Z-matrix. The computational time for an N-segment problem is given by:

$t=AN^2+BN^3$

Where A is a machine dependent coefficient related to filling the matrix; and B is a machine dependent coefficient related to factoring the matrix.

Note: Normally the coefficient A is much larger than B which means that the N^2 term dominates in smaller problems. At some point (typically between 100 and 300 segments) however the N^3 term starts to dominate, resulting in severe penalties for any increase in problem size. This is the ultimate factor limiting the applicability of the MM to Electrically large problems theoretically the technique is suitable for any size problem with the upper limit always dictated by available computer speed and memory.
The time taken to calculate M field points may also be large if many field points are required. This time is given by:-
$t=CMN$

Where C is a machine dependent constant.

The memory required for a solution is once again dominated by the matrix storage requirement. The Z-matrix is complex and normally real numbers in computers are represented in a 4-byte format hence:

Memory=$8N^2$

Normally it is desirable to have this amount of memory available in core storage since disk swap operations slow down execution considerably [Fourie 91].

1.2 Geometric theory of diffraction

One of the most versatile and useful high frequency techniques is the geometric theory of diffraction (GTD), which was developed around 1951 by J.B Keller [Lo 93]. Geometric theory of diffraction is based on modern physics, where rays are reflected and diffracted from surfaces and edges. The trajectories of a ray can be computed by using the law of reflection or Snells law of refraction.

The GTD approach is ideal for a general high frequency study of antennas in a complex environment in that only the most basic structural features of an otherwise very complicated structures need to be modelled. This is because ray optical techniques are used to determine components of the field incident on and diffracted by various structures. Components of the diffracted fields are found using the GTD solutions in terms of the individual rays, which are summed with the geometrical optics terms in the far field. The rays from a given scatter tend to interact with other structures causing various higher order terms. In this way one can trace out the various possible combinations of rays that interact between scatters and determine and include only the dominant terms. This method leads to accurate and efficient computer codes that can be systematically written and tested. Complex problems can be built up from simpler problems in manageable pieces [Marhefka 79]

This section will give a brief overview of the properties of a high frequency field and some special cases, based on figure 5. Figure 5 shows an infinitesimally narrow ray tube positioned about some central ray with ray vector s and along which the distance s is measured, with two closely spaced equiphase surfaces $\Psi(O)$ and $\Psi(s)$ a distance s apart. [1]

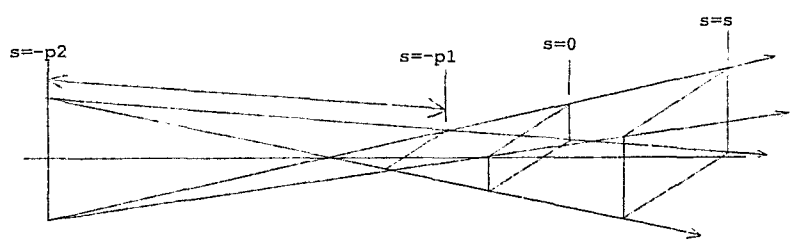


Figure 5: Infinitesimally narrow diverging astigmatic ray tube, for which both ρ1 and ρ2 are positive (ρ is the astigmatic difference).

The expression describing the transmission of the g ometrical optics (GO) field, for the general astigmatic ray tube shown in figure 5 is given by,

$$E(s) = E(0)\sqrt{|\rho 1 \rho 2/(\rho 1+s)(\rho 2+s)|}e^{-jks}e^{j(n-m)\pi/2} \qquad (2.1)$$

Where:
a) E(0) gives the field amplitude, phase and polarization at the reference point s=0.

b) S is the distance along the ray path from the reference point s=0, and hence

c) e^{-jks} gives the phase shift along the ray path.

d) The term A(s) = $\sqrt{|\rho 1\rho 2/(\rho 1+s)(\rho 2+s)|}$ (2. 2)

is the divergence factor (or spreading factor), which governs the amplitude variation of the GO field along the ray path.

e) ρ1 and ρ2 are the principle radii of curvature of the wavefront (which is a surface) at the reference point s=0. The sign convention is that a positive (negative) radius of curvature implies diverging (converging) rays in the corresponding principal plane.

f) n is the number of caustic lines crossed by the observer in moving from the reference position s=0 to the given observation points s in a direction of propagation. M is in the opposite direction of propagation.

All of these considerations have been given in terms of E, but

$$H(s)=H(0)\sqrt{|\rho 1\rho 2/(\rho 1+s)(\rho 2+s)|}e^{-jks}e^{j(n-m)\pi/2} \quad (2.3)$$

Is equally valid, with H(s) and E(s) related locally by the expression:

$$H(s)=Ys\times E(s) \quad (2.4)$$

With

$$Y=\sqrt{\varepsilon_0\varepsilon_r/\mu_0}$$

Three special cases, namely a plane wave ray tube, a cylindrical wave ray tube, and a spherical wave ray tube, are described below using equation 2.1 or 2.3.

Plane wave ray tube

Suppose we are interested in the case for which the surface of constant phase, at the selected reference point, is planar. This means that in (2.1) we must let the radii of curvature ρ1 → ∞ and ρ2 → ∞. As a consequence the spreading factor in (2.2) reduces to A(s) =1, and there is no variation of the amplitude with s along the ray path and the wavefront remains planar.

The expression for such a GO field simplifies to

$$E(s) = E(0)e^{-jks} \tag{2. 5}$$

Cylindrical Wave Ray Tube

In a cylindrical wave ray tube one of the principal radii of curvature is infinite whereas the other is finite, at some reference point. Therefore let $\rho 1 \rightarrow \infty$ and $\rho 2 \rightarrow \rho$, with ρ being a finite value. The divergence (spreading) factor (2.2) then becomes

$$A(s) = \sqrt{\rho/(\rho+s)}$$

The general astigmatic ray tube expression (2.1) therefore simply is

$$E(s) = E(0)\sqrt{\left|\rho/(\rho+s)\right|}e^{-jks} \tag{2. 6}$$

To refer the field to the caustic line at s= -ρ (equivalent to letting $\rho \rightarrow 0$) often is convenient, although we cannot use (2.6) to evaluate the field there. To achieve this, the amplitude of the ray tube field is examined by taking the modules of either side of (2.6):

$$E(s) = \left|E(0)\right|\left|\sqrt{\rho}\right|/\left|\sqrt{\rho+s}\right| \tag{2. 7}$$

We then recognise that the field amplitude E(s) in (2.7), for fixed s, must be a constant irrespective of the reference position. Next, (2.7) is rewritten as

$$E(s)\left|\sqrt{\rho+s}\right| = \left|E(0)\right|\left|\sqrt{\rho}\right| \tag{2. 8}$$

Clearly, as $\rho \rightarrow 0$ (I.e., the reference position is shifted to the caustic line) for fixed s the left handed side of (2.8) becomes $|E(s)|\,|\sqrt{s}|$, which also is a constant, e.g., A_0, and so will the right hand side $|E(0)|\,|\sqrt{\rho}|$. In other words, when $\rho \rightarrow 0$ expression (2.7) becomes

$$\left|E(s)\right| = \frac{A_0}{\sqrt{s}} \tag{2. 9}$$

Incorporating the phase at the reference point, as well as the vector properties, into a constant vector quantity A_0, for example, the complete expression for the cylindrical wave ray tube, with reference position at the caustic line and s the distance from this caustic line, simply is

$$E(s) = A_0 \frac{e^{-jks}}{\sqrt{s}} \tag{2. 10}$$

the cylindrical source.

Spherical Wave Ray Tube

If ρ1 = ρ2 = ρ, for example, we have the case of a spherical wave ray tube. The spreading factor A(s) then reduces to the form A(s)= ρ/(ρ+s), and the field expression is given by

$$E(s) = E(0)\frac{\rho}{(\rho + s)}e^{-jks} \qquad \textbf{(2. 11)}$$

If we wish to refer the field to the caustic at s = -ρ, then, following arguments similar to those for the cylindrical wave ray tube, we obtain the expression:

$$E(s) = A_0 e^{-jks} / s \qquad \textbf{(2. 12)}$$

And the same comments regarding the terms A_0 can be made [McNamara 90].

This has been a very brief overview of some GTD concepts, for further information regarding GTD and the GO theories, please consult the references given.

2 Modelling guidelines

The advice tendered in the NEC users guide [Burke 81] as well as by trueman et al [Trueman 90] are shown in table 1. If a wire grid which, violates NEC's basic assumptions, is input to the program, no warning is given. NEC computes currents and fields, which may be physically meaningless and quit misleading. The modelling guidelines help to identify those structures, which NEC can solve correctly, and conversely point out structures for which NEC is not likely to obtain a correct solution. The " modelling guidelines" can be regarded as " necessary conditions" for NEC to correctly solve for the currents on a wire grid structure. But they are not sufficient conditions for if a wire grid model satisfies the modelling guidelines, the wire grid is not necessarily a good electrical representation of the surface (see the section on the equal area rule).

Table 1 [7]

Δ = Segment length

a = wire radius

λ = Wavelength

Individual segments	Warning	Error
Segment length	$\lambda/10<\Delta<\lambda/5$	$\Delta>\lambda/5$
Radius	$30<\lambda/a<100$	$\lambda/a<30$
Segment to radius ratio	$0.5<\Delta/a<2$	$\Delta/a<0.5$
Junctions		
Segment length ratio		$\Delta_{big}/\Delta_{small}>5$
Radius ratio	$5<a_{big}/a_{small}<10$	$a_{big}/a_{small}>10$
Segment to radius ratio	$2<\Delta/a<6$	$\Delta/a<2$

Match point	Segment center within half a wire radius of another wire's surface	Segment center lies within the volume of another wire
Wire spacing		
Crossed wires		Wire axis cross
Overlaps		Wire axes pass closer than the sum of the wire radii
Near misses	Wire axes pass closer than 1.5 times the sum of the wire radii	
Proximity	Wire endpoints closer than 1.5 times the sum of the wire radii	Wire endpoints closer than the sum of the wire radii

Equal area rule

For an orthogonal grid of wires representing a solid surface, the segment length determines the "cell size" of the wire grid. The highest frequency of interest usually determines the segment length: it is set at 0.10λ or perhaps 0.14λ at that frequency. The radius is then chosen according to the "equal surface area rule" [Ludwig 87, Mayhan 90], stating that the total surface area of the wires in one direction is made equal to the area of the surface. For a square grid cell of side length Δ, the "equal area rule" radius is $\Delta/2\pi$. [Trueman 90]

For a plate one λ by one λ square, at a frequency of 640MHz, and with segments of $\lambda/10$ long, the radius of the wires can be calculated as follows.

$$\sum 2\pi rl = 2 \times l \times b$$

And as there as 22 wires the equation above becomes:-

$$44\pi r\lambda = 2\lambda^2$$

$1/r = 22\pi/\lambda$

and

$r = \lambda/22\pi$

And as $\lambda = 300/f = 300/640$

$$\lambda = 468\text{mm}$$

Therefore: $r = 0.468/22\pi = 6.77\text{mm}$

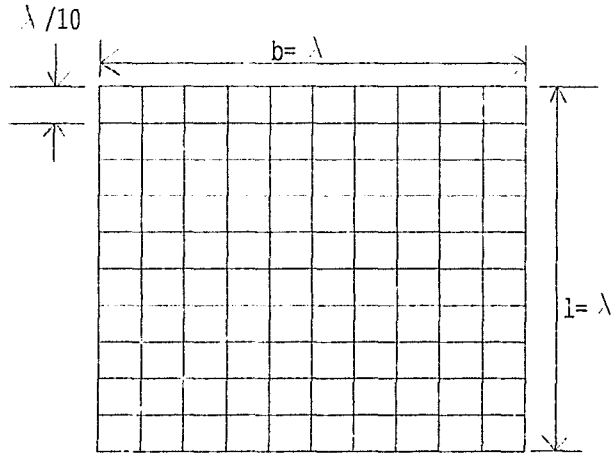


Figure 6: Gridded Plate for MOM simulation

3 Anechoic chamber measurements

The anechoic chamber is a room in which energy incident on the walls is either absorbed or, more likely, directed away from the area occupied by the antenna under test [Burberry 92].

The purpose of an anechoic (no echo) chamber is to simulate a reflection-less free-space environment in which the interaction between electromagnetic waves and many different devices can be investigated under controlled conditions.

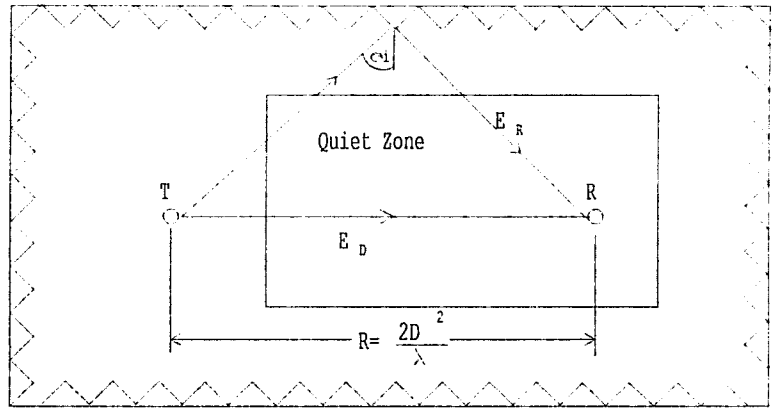


Figure 7: Rectangular chamber [Rudge 82]

Figure 7 above shows a rectangular chamber. In an antenna pattern or gain measurement a directive illuminating antenna T is usually placed near the middle of one of the end walls of the chamber. The test antenna R is placed at a distance R from the illuminating antenna. This sets up a direct field E_D as well as a reflected field E_R. Generally in the design of a rectangular chamber the level of the reflected signal is required to be below a certain specified value in the quiet zone, placed around the antenna. To achieve this quiet zone the distance R must be greater than $2D^2/\lambda$. Here, D is the diameter of the test antenna and λ is the wavelength. Since in practice upper limits exist on the length, width and height if chambers, there exists also a limit on the ratio D^2/λ of antennas which can be tested using conventional methods. The required low level of reflections also influences the dimensions of the chamber. The chamber width and height should be such that the indicated angle of incidence θ_i on the longitudinal surfaces of the chamber is less than about 60°. A larger angle of incidence will cause large reflections from the absorbers. In the assessment of the total length of the chamber, it has to be taken into account that the test antenna should be placed at a distance, from the tips of the end-wall absorbers, equal to half the distance between the tips

of the side-wall absorbers. This is done in order to reduce the influence of reflections from the end wall absorbers including coupling between the absorbers and the test antenna. These considerations lead to a length to width ratio of about 2:1. Often, with the result of larger reflections but in order to satisfy the far field criterion without having a large width, a length to width ratio of 3:1 is accepted.

Absorbing material has been developed to operate in the frequency range from 100MHz to 100GHz. At the lower frequency, reflection coefficients of –40dB have been obtained. At angles of 60°, reflection coefficients of about-25dB may have to be accepted. The ideal absorber has an impedance equal to air at the air-absorber interface. In order to convert the electromagnetic energy into heat, the absorbers are manufactured of dielectric and/or magnetic material with loss. Since there should be a smooth impedance variation from the air absorber interface to the metal plate on which the absorbers are usually mounted, most absorbers utilise a resistive taper which is obtained either geometrically (e.g. pyramidal absorbers) or electrically (e.g. absorbers made of alternating layers). High performance absorbers should have a good impedance match over a wide frequency band for a large range of angles of incidence, The present day polyurethane foam absorbers loaded with carbon may be up to a few metres in length. Thin ferrite absorbers may be used, but they are costly and may be too frequency sensitive [Rudge 82].

4 Reference

Burberry R.A. 'VHF and UHF Antennas' 1992

Burke G.J., Pagio A.J. 'Numerical Electromagnetics Code (NEC) – Method of Moments' 1981

Fourie A. ' Introductory course on method of moments EM simulation using the numerical electromagnetic code NEC2' 1991

Lo Y.T., Lee S.W. 'Antenna handbook vol1' 1993 Pathak chapter 4 'Techniques for high frequency problems'

Ludwig A.C. 'Wire grid modelling of surfaces' IEEE Transactions on Antennas and Propagation. Vol AP-35, No. 9 Sept 1987.

Marhefka R.J., Burnside W.D. 'Numerical Electromagnetic Code (NEC)-Basic Scattering code part1 users manual' 1979 BSCAT

Mayhan J.T. ' Characteristic Modes and Wire and Wire grid modelling' IEEE Transactions on Antennas and Propagation. Vol 38, No. 4 April 1990.

McNamara D.A. , Pistorius C.W.I., Malherbe J.A.G. 'Introduction to the Uniform Geometrical Theory of Diffraction' 1990

Rudge A.W., Milne K., Olver A.D., Knight P. 'The Handbook of Antenna Design – Volume 1' 1982

Thiele G.A., Newhouse T.H. 'A Hybrid Technique for Combing Moment Methods with the Geometrical Theory of Diffraction' IEEE Transactions on Antennas and Propagation Vol AP-23 Jan 1975

Trueman C.W., Kubina S.J. 'Verifying Wire-Grid Modelling Integrity with program "check". ACES Journal Vol 5, No.2 1990.

Appendix B : 357 MHz Dipole

1 357MHz Dipole

The reason for the reconstruction and re-testing of the 357MHz dipole, was to determine the accuracy of the measurements to be done, and, also, to obtain a dipole with a known accuracy which can be scaled to suit any required frequency.

The Dipole used, as a basis for further work, is the one, which has been documented by J. Dresel et al [Dresel 96]. Careful construction and calibration of the dipole was required in order for accurate measurements to be done. The dipole has been constructed as in figure 1, with dimension given in table 1 below. Note that the dipole overlaps the edge of the wooden boom to reduce interference to the dipole from any materials. The wooden boom apart from acting as a support for the structure, also allowed for an easy attachment of the cable which should be kept well back from the dipole during measurements.

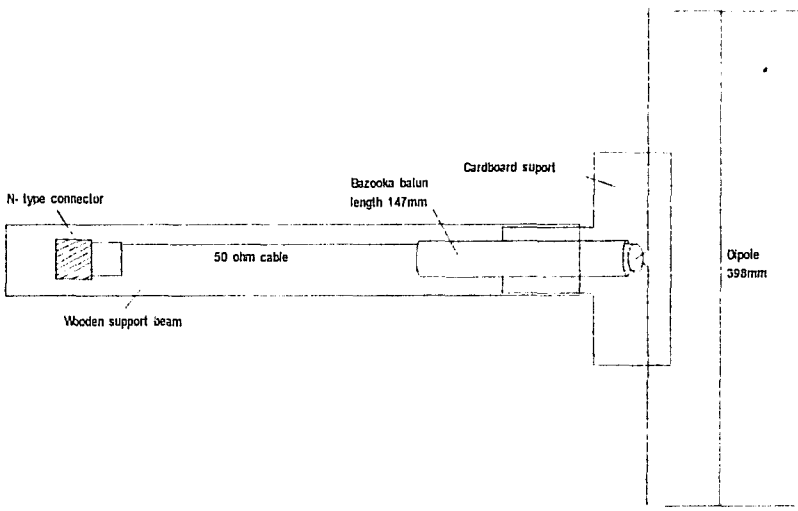


Figure 1: Construction of the 357MHz dipole and assembly

	Dipole length (mm)	Balun length (mm)
357Mhz (actual)	398mm	147mm
357MHz (theoretical)	420mm	156mm

Table 1: Comparison of the dimension for the actual 357MHz dipole and theoretical values.

The dipole, once constructed, was then placed in an anechoic chamber and following the calibration procedures listed in the literature survey on impedance measurements, the cable losses were then calibrated out, at the feed point of the dipole. The impedance was measured over a span of 100MHz which is wide

enough to allow for any frequency offsets but small enough that the calibration is accurate over the range, bearing in mind that the analyser used, only measures a certain number of points. Once the data had been obtained the data was then analysed using MATLAB.

From table 1 it can be seen that the actual antenna dimensions are different from those which would have been expected, for instance, the $\lambda/2$ dipole should be 420mm, but is instead 398mm, which is about 5% smaller. The $\lambda/4$ balun, on the other hand, taking into account the 0.66 velocity factor associated with the coaxial cable, is calculated to be 138mm, but instead is 147mm, which is 6% larger.

Figure 2 shows the results obtained in Smith Chart form, with Figure 3 and 4 giving a more detailed view of the real and imaginary impedances, respectively. As can be seen in Figures 3 and 4 the balun is actively working over a range of approximately 10% from the centre frequency, with the centre frequency being at about 357Mhz. Outside the 10% bandwidth the measured results tend to diverge from the simulated patterns.

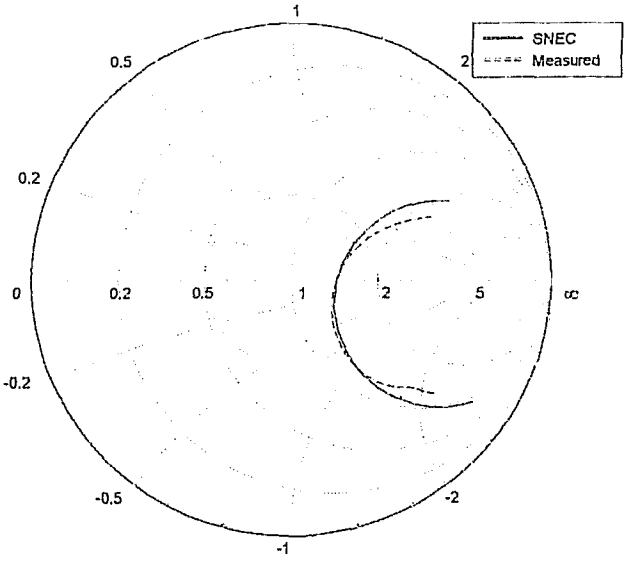


Figure 2: Smith Chart of the simulated versus the measured impedance values.

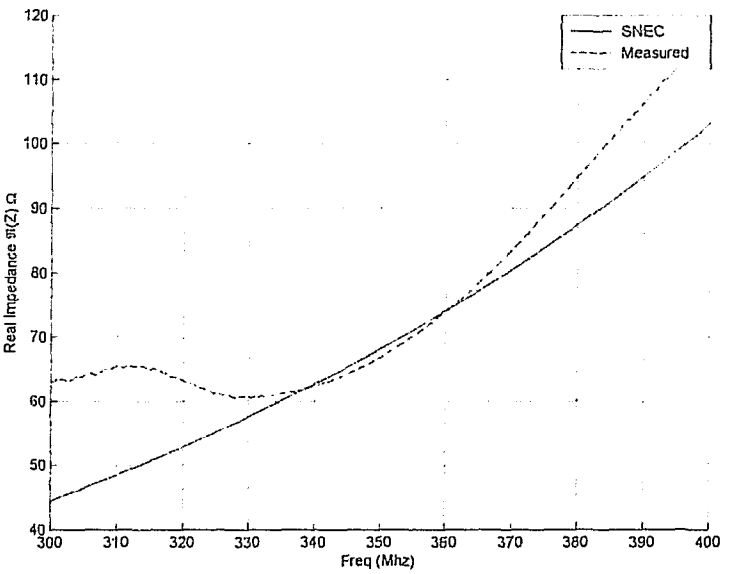


Figure 3: Comparison of the real impedance from the simulated and measured values.

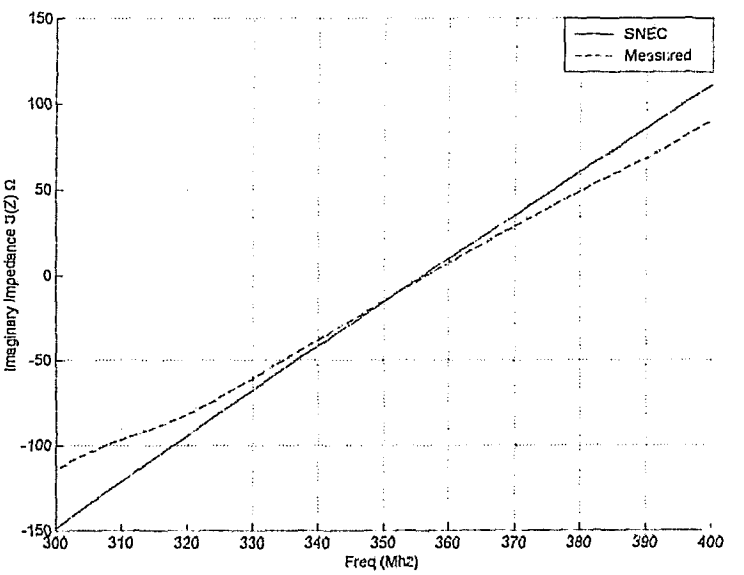


Figure 4: Comparison of the Imaginary impedance from the simulated and measured values.

2 Conclusions

The results obtained for the 357MHz dipole confirm that extremely accurate comparisons can be made between the simulated and measured data of a dipole, provided that the dipole is accurate made as well as calibrated.
As accurate results have been obtained, the dipole dimensions can be scaled to the frequency of interest.

3 References

Dresel J, Fourie APC, Givati O, Clark AR ' The Modelling of Lossy Surfaces using a Wire Method of Moments Code' Symposium on Antenna Technology and Applied Electromagnetics, 1996 Conference Proceedings, Aug 6-9.

Appendix C : 450 and 600MHZ Dipole

1 *Dipole 450 and 600MHz*

The 450MHz and 600Mhz dipole, shown in figure 1 below, were simulated using SNEC and then measurements taken of the radiation pattern and the impedance. The purpose of producing both a 450 and 600MHz dipole was for repeatability of scaling Dresel's dipole (see Appendix B). Without an accurate model for measurements it would be difficult to say for certain if SNEC gives accurate results for either MOM or GTD.

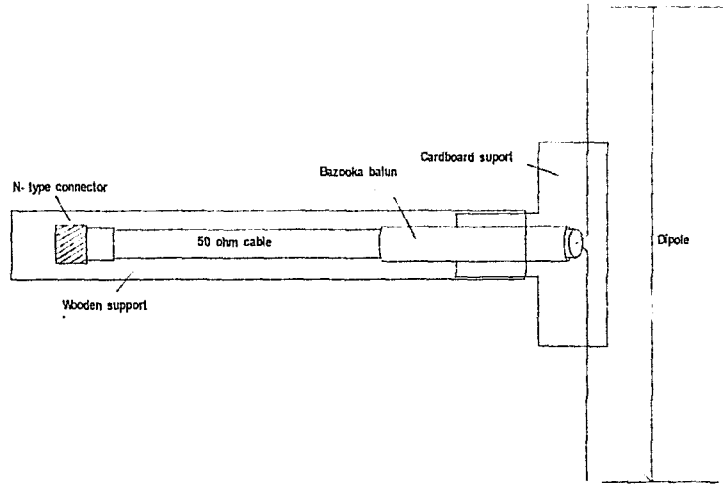


Figure 1: 450MHz and 600MHz dipole construction

The dimensions of the theoretical dipoles and baluns are shown in table 1 below:

	Dipole length (mm)	Balun length (mm) VF=0.66
450MHz	333	110
600MHz	250	82.5

Table 1: Dimensions of the theoretical 450 and 600MHz dipoles

As mentioned in Appendix B, the lengths given in table 1 are different from the actual λ/2 and λ/4, shown in table 2, by certain percentages.

	Dipole length (mm)	Balun length (mm)
450MHz	298	110
600MHz	222	82

Table 2: Actual dimensions used for the 450 and 600MHz dipoles

With the above dimensions excellent correlation between simulated and measured results were obtained over the balun 'working' range, as shown in figures 2 below.

The results obtained using the dimensions in table 2 were as accurate as was obtained in a previous (Appendix B). Figure 2 shows the Smith Chart for the 450MHz dipole with figure 3 and 4 showing the real and imaginary impedance. The 10% bandwidth over which the balun is working properly can be clearly seen.

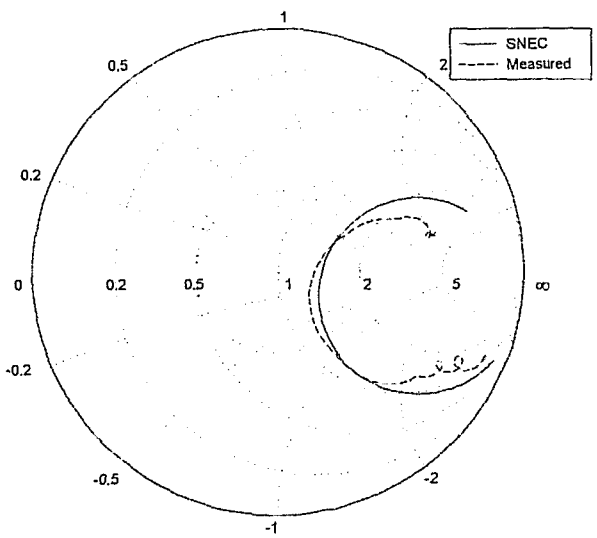


Figure 2: Smith Chart of the 450Mhz dipole, showing the impedance changes over the frequency range 300MHz to 500MHz

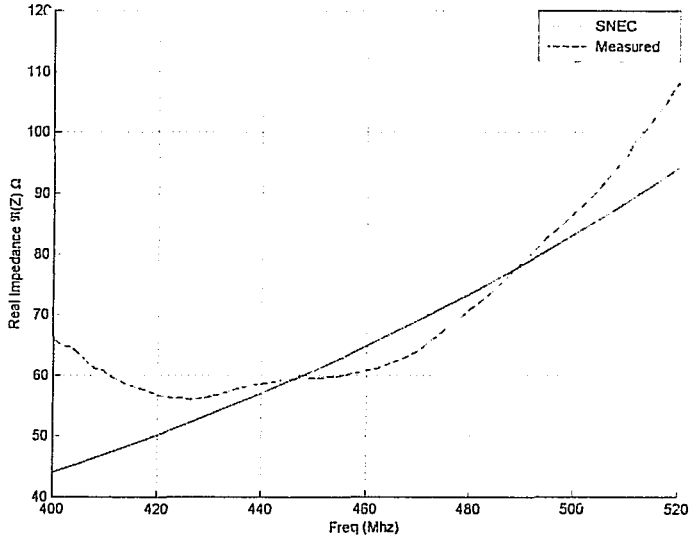


Figure 3: Real impedance of the 450MHz dipole

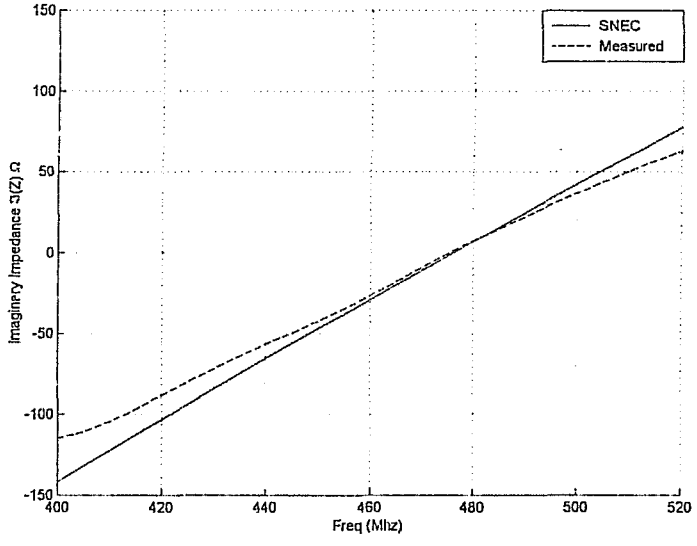


Figure 4: Imaginary impedance of the 450MHz dipole

From the imaginary plot in figure 4 it can be seen that the resonant frequency is actually round about 470MHz. The balun appears to give accurate results from about 440 to 500MHz, before the measurement error becomes to great to use.

Once again the 600MHz dipole has been scaled from the 357MHz dipole with extremely good comparisons between the simulated and measured data being achieved.

Figure 5 shows the smith chart for the 600MHz dipole with a more detailed view of the real and imaginary impedance's given in figures 6 and 7 respectively.

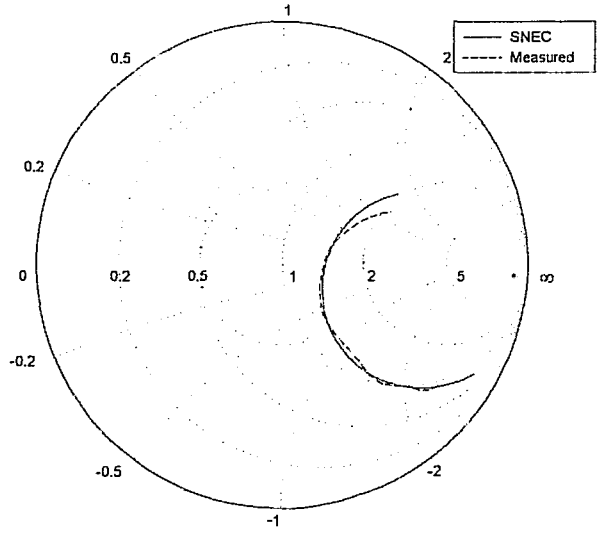


Figure 5: Smith Chart of the 600MHz dipole over the range 500 to 700MHz

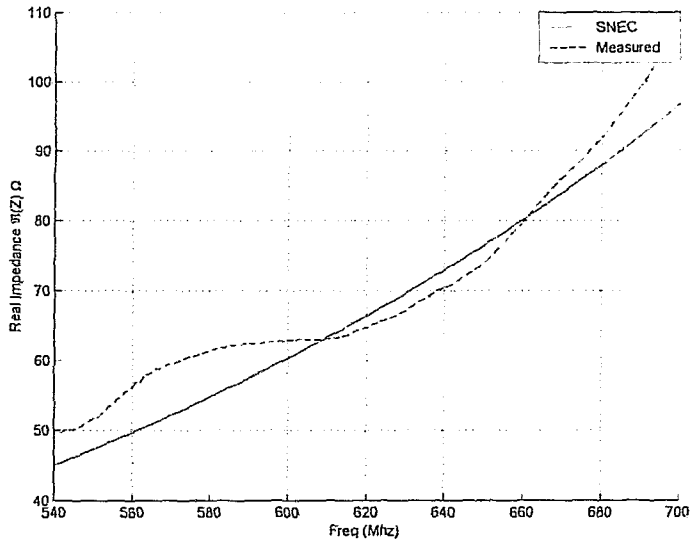


Figure 6: Real impedance of the 600MHz dipole

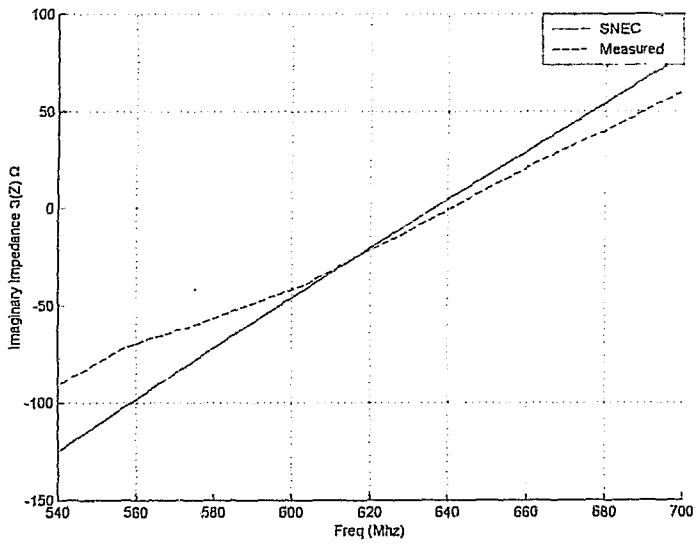


Figure 7: Imaginary impedance of the 600MHz dipole, showing the resonant frequency at 640MHz

2 Conclusion

As there is a discrepancy between the calculated dimensions of the dipole and balun and the actual dimension required for accurate measurements, more research needs to be done into balun measurements.

Other problems encountered during measurement were found to be caused by the type of resistors used in the calibration technique. Surface mount resistors were found to give the most accurate results, due to their small size. The feeder cable also required careful positioning in order to reduce interference. A wooden boom was used where the feeder cable was attached and taken back as far from the dipole as possible reducing the interference created by the feeder cable.

Appendix D : Dipole and Reflector Plate

1 Dipole and plate

A dipole in front of a reflector plate is a good method of determining the accuracy of the GTD compared to MOM. As the reflector plate can be simulated using MOM by creating the plate from small segments and keeping to the gridding rules [Ludwig 87, Mayhan 90]. The plate in the GTD model is created from a sheet of the correct dimensions. A physical structure of the reflector plate and dipole has been construction to give a comparison between measurements, and MOM and GTD in SNEC.

Figure 1 shows the construction of the plate and dipole with dimensions. The plate was made of 1mm thick aluminium plate, 468mm (λ) square. The used is the same 600MHz dipole as in Appendix C. The dipole is placed λ/4 away from the plate.

The plate dimension has been chosen as it is on the limits of both MOM and GTD. The plate is fairly large for MOM simulation but small for as GTD simulation. As SNEC combines both MOM and GTD the results would be of interest to those who want to simulate structures with both small and large structures combined.

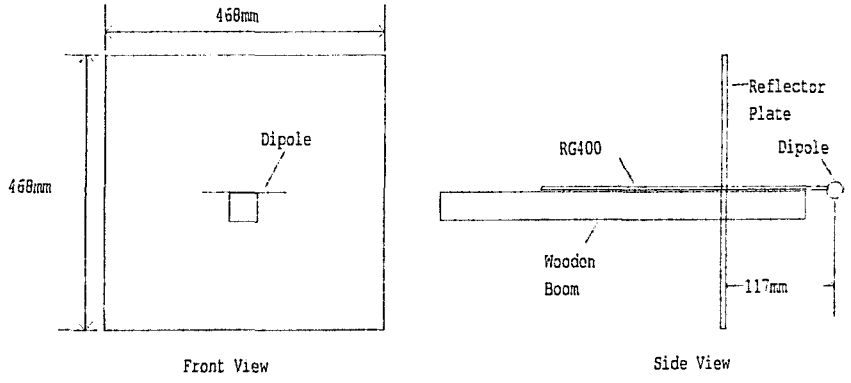


Figure 1: Dimensions of the dipole and reflector plate

Firstly the plate and the 600MHz dipole were simulated using MOM. The grid has been made with each segment being λ/10 in length, as shown in figure 2.

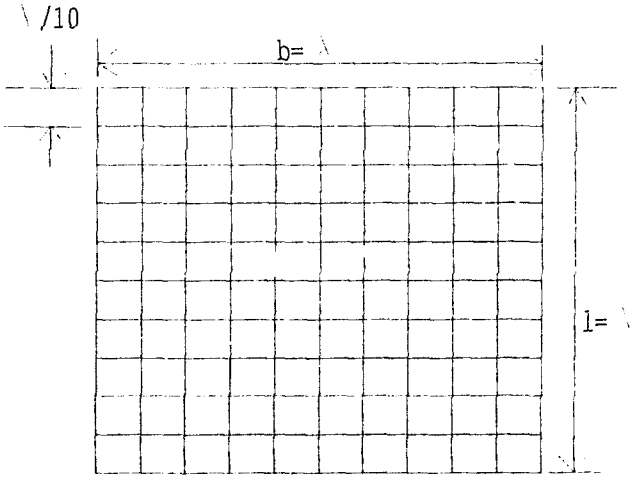


Figure 2: Segmented plate for MOM simulation

As can be seen in figure 2 there are 220 segments which make up the λ by λ plate. As the plate is made bigger so does the amount of segments increase, thereby increasing the computer processing power required. As the structure increases to a size, which is difficult to simulate using MOM, so does the GTD structure become more advantageous to use. The GTD plate, as mentioned in Appendix A, is made from a single plate, which must be large enough for the waves to be planar. The code for both the MOM simulation and the GTD are listed below as code 1 and code 2 respectively.

CM Dipole behind plate, one wavelength long and wide (468mm)
CE dipole at 640Mhz, Length =222mm

GW 1	10	-0.2340	0.	-0.2340	0.2340	0.	-0.2340	0.0067
GW 2	10	-0.2340	0.	-0.1872	0.2340	0.	-0.1872	0.0067
GW 3	10	-0.2340	0.	-0.1404	0.2340	0.	-0.1404	0.0067
GW 4	10	-0.2340	0.	-0.0936	0.2340	0.	-0.0936	0.0067
GW 5	10	-0.2340	0.	-0.0468	0.2340	0.	-0.0468	0.0067
GW 6	10	-0.2340	0.	0.0000	0.2340	0.	0.0000	0.0067
GW 7	10	-0.2340	0.	0.0468	0.2340	0.	0.0468	0.0067
GW 8	10	-0.2340	0.	0.0936	0.2340	0.	0.0936	0.0067
GW 9	10	-0.2340	0.	0.1404	0.2340	0.	0.1404	0.0067
GW 10	10	-0.2340	0.	0.1872	0.2340	0.	0.1872	0.0067
GW 11	10	-0.2340	0.	0.2340	0.2340	0.	0.2340	0.0067

```
GW 12  10 -0.2340  0.    -0.2340  -0.2340  0.    0.2340  0.0067
GW 13  10 -0.1872  0.    -0.2340  -0.1872  0.    0.2340  0.0067
GW 14  10 -0.1404  0.    -0.2340  -0.1404  0.    0.2340  0.0067
GW 15  10 -0.0936  0.    -0.2340  -0.0936  0.    0.2340  0.0067
GW 16  10 -0.0468  0.    -0.2340  -0.0468  0.    0.2340  0.0067
GW 17  10  0.0000  0.    -0.2340   0.0000  0.    0.2340  0.0067
GW 18  10  0.0468  0.    -0.2340   0.0468  0.    0.2340  0.0067
GW 19  10  0.0936  0.    -0.2340   0.0936  0.    0.2340  0.0067
GW 20  10  0.1404  0.    -0.2340   0.1404  0.    0.2340  0.0067
GW 21  10  0.1872  0.    -0.2340   0.1872  0.    0.2340  0.0067
GW 22  10  0.2340  0.    -0.2340   0.2340  0.    0.2340  0.0067
GW 23  11 -0.1110  0.117   0.0     0.1110  0.117   0.0     0.0008
GE 0
FR 0  3  0  0   640.0    20.
EX 0  23  6  0    1.0     0.0
RP 0 361  1 1010    0.    90.    1.    0.
RP 0  1 361 1010   90.     0.    0.    1.
XQ
EN
```

Code 1: MOM code for Plate and dipole

```
CM Dipole behind plate, one wavelength long and wide (468mm)
CE dipole a 600Mhz, Length =222mm
PL 2  0  4  0
CR 2  1 -0.234 0.  0.234
CR 2  1  0.234 0.  0.234
CR 2  1  0.234 0. -0.234
CR 2  1 -0.234 0. -0.234
GW 23  11 -0.1110  0.117   0.0     0.1110  0.117   0.0     0.0008
GE 0
FR 0  3  0  0   620.0    20.
EX 0  23  6  0    1.0     0.0
RP 0 361  1 1010    0.    90.    1.    0.
XQ
EN
```

Code 2: GTD code for Plate and dipole

AS can be seen in code above, code 1 is still the same as that used in NEC and NEC2 [Pogio 81]. Code 2 is much simpler than the code for a MOM plate in code 1. The plate in GTD is constructed using PL and CR, with the dipole still being constructed using MOM. PL is used to construct the plate

and CR is used to set the size and which sides will be used for reflections [Nitch 98].

Figure 3 shows the impedance for the plate and dipole, comparing MOM, GTD and measured results. The simulated results compare excellently with the measured results being only good over the range of the balun, which is approximately 10%. Figures 4 and 5 show more detail in the real and imaginary parts of the impedance.

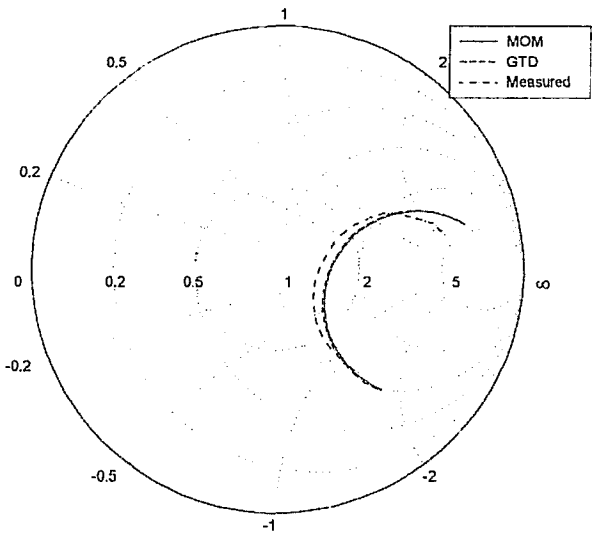


Figure 3: Smith Chart for the MOM, GTD and Measured data

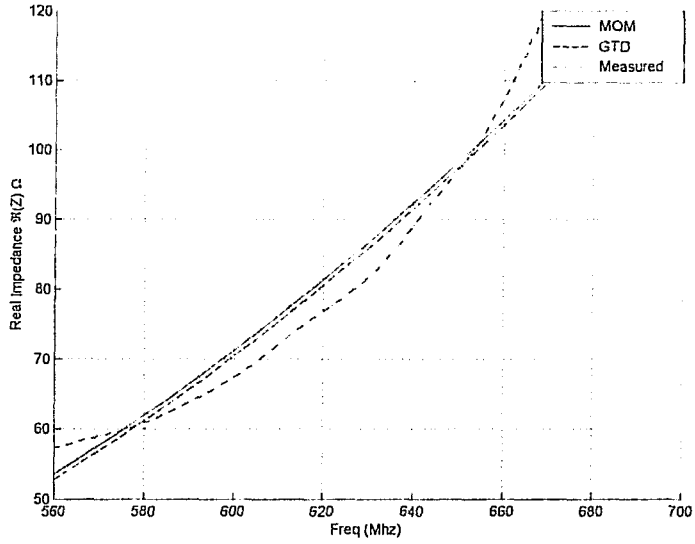


Figure 4: Real impedance of the MOM, GTD and measured data.

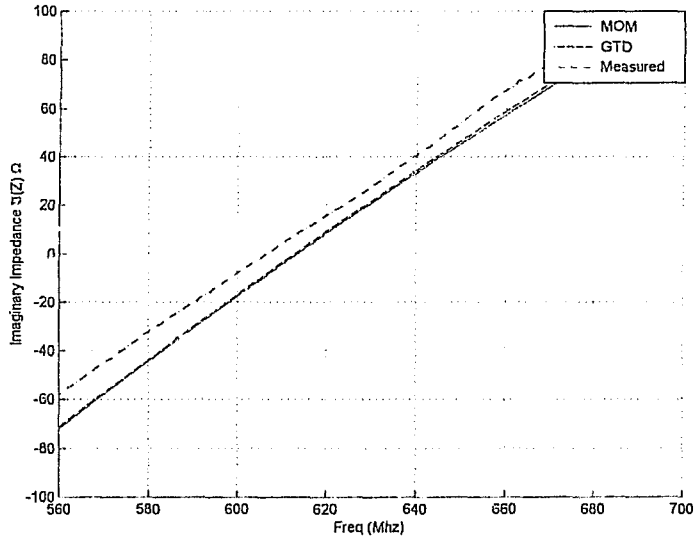


Figure 5: Imaginary impedance of the MOM, GTD and measured data

Figures 6, 7, and 8 show the radiation patterns of the dipole and plate at the frequencies 620, 640 and 660MHz. The results for the MOM and GTD plate are almost identical, whereas there is a larger discrepancy with the measured values. The measured values do, however, compare closer with the MOM and GTD results at 600MHz, which is probably due to the working range of the balun.

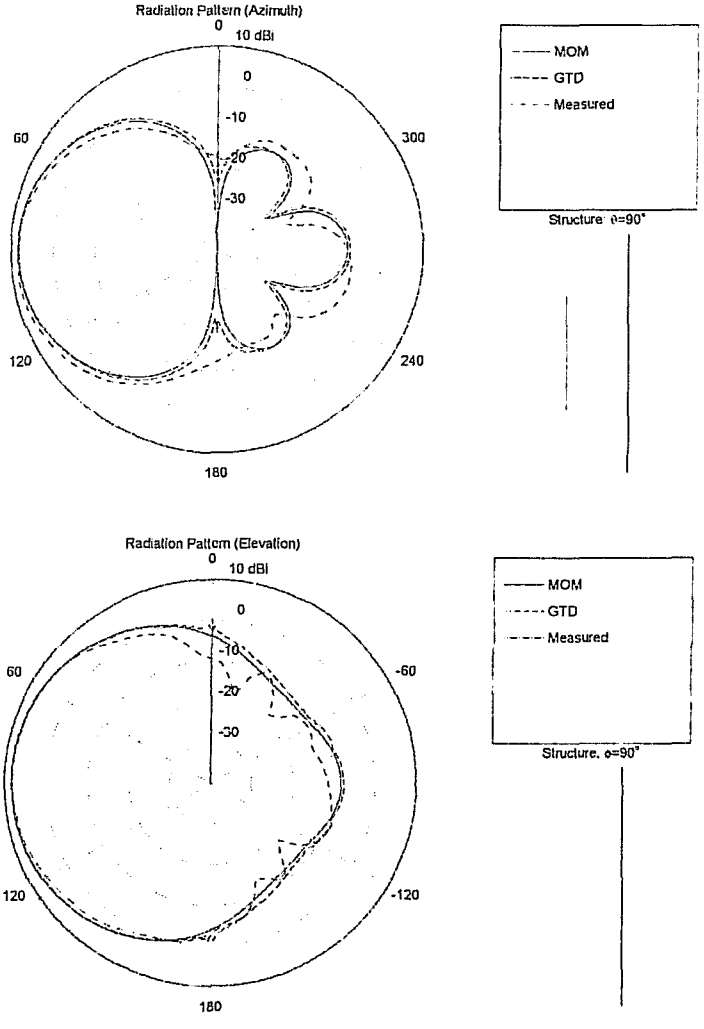


Figure 6: Radiation patterns for the dipole and plate at 620MHz, showing the elevation and azimuth planes

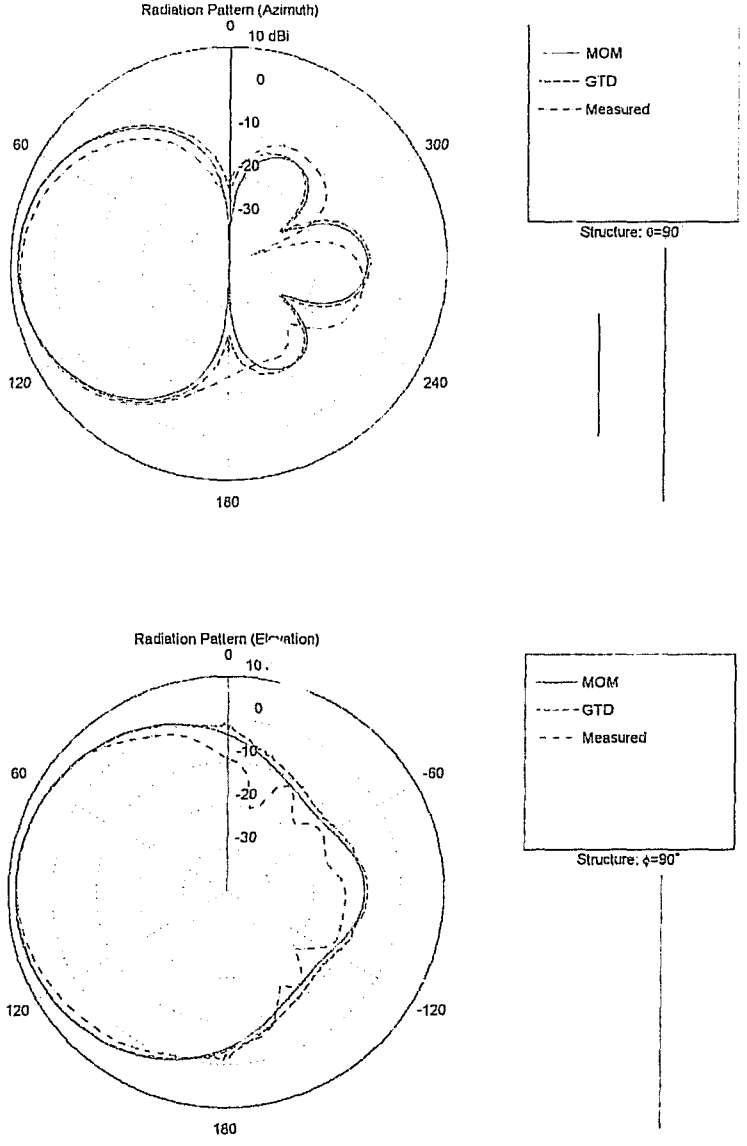


Figure 7: Radiation patterns for the dipole and plate at 640MHz, showing the elevation and azimuth planes

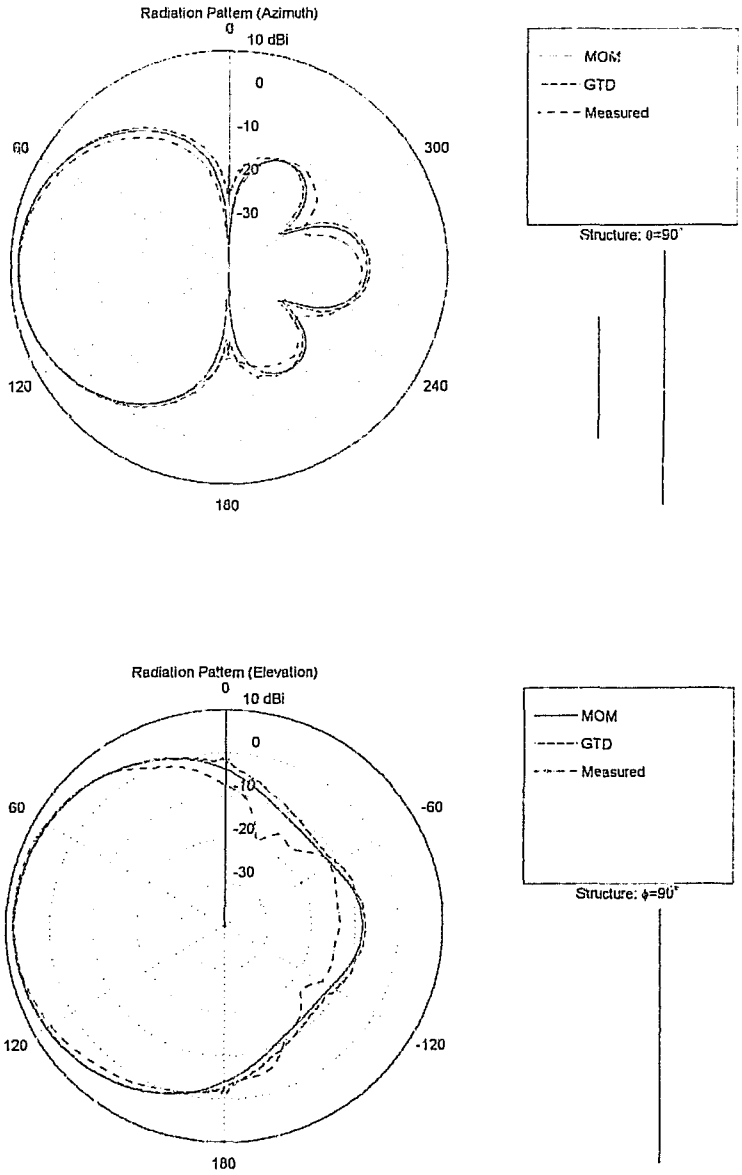


Figure 8: Radiation patterns for the dipole and plate at 660MHz, showing the elevation and azimuth planes

2 Conclusion

SNEC appears to give accurate results when either MOM or GTD are used, even for a plate of size, λ by λ. The measurements are the least accurate followed by the GTD, with MOM giving the best results. These results do confirm the findings by Kraus [Kraus 88]. There are small anomalies in the radiation patterns produced in the GTD model, at 90 and 270 degrees, which do not effect the usability of the patterns in any way, as long as you know that they are there and that they are caused by the simulation. Hopefully these anomalies will be eliminated in future versions.

3 References

Kraus J.D. 'Antennas second edition' 1988

Ludwig C.A. 'Wire Grid Modelling of Surfaces' IEEE transactions on antennas and propagation, VOL. AP-35, NO. 9, September 1987

Mayhan J.T. ' Characteristics Modes and Wire Grid Modelling' IEEE Transactions on antennas and propagation, Vol.38, No. 4, April 1990

Nitch D. 'Super Nec MOM-GTD Hybrid User Reference Manual' February 1998

Pogio A.J. and Burke G.J. 'Numerical Electromagnetic Code (NEC) – Method of Moments' Naval Ocean Systems Centre Technical document 116 Volume 1 January 1981

Appendix E : GTD/MOM Hybrid

1 MOM/GTD Interaction Matrix

A combination of the GTD and MOM, has been attempted by firstly placing a 0.5 by 0.5λ plate in the centre of a λ by λ, whereby the rest of the plate is made up of a grid. The next step was to reverse the GTD and MOM, by placing the grid on the inside of the plate and the GTD plate on the outer edges. The third iteration has been run as in the first iteration, but the inside plate has been enlarged to 0.8 by 0.8λ A fourth simulation was run to confirm the conclusions made from the previous iteration and consisted firstly of a 1λ by 1λ and then a 1.6λ by 1.6λ plate, inside a grid 2λ by 2λ.

The reason for attempting the interaction between MOM and GTD on a plate is to gain some feedback on whether it is possible to use GTD on the less important areas and MOM on the more detailed sections. The interaction matrix will allow the user to reduce the permutations on larger structures, which require large amount of segments, and therefore computer power.

Figure 1 shows the construction of the plate, combining MOM and GTD. Figure 1 a shows the plate gridded using MOM on the outside and GTD solid plate on the inside. Figure 1 b is the inverse with the GTD plate being on the edges and the grid in the centre.

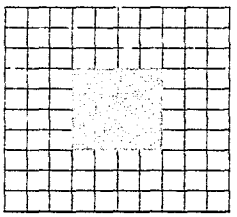


Figure 1 (a)

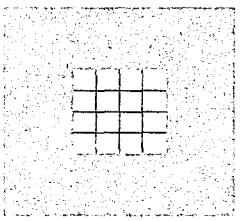


Figure 1 (b)

Firstly the simulation was run with the inner half as a GTD plate and the outer section made of a MOM grid. The results gave no real comparison to the simple GTD or simple MOM plate and dipole, no matter which reflections and diffraction terms were turned on or off.

Figure 2 shows the radiation patterns generated in SNEC for the Plate and 600MHz dipole, as shown in figure 1a.

1 MOM/GTD Interaction Matrix

A combination of the GTD and MOM, has been attempted by firstly placing a 0.5 by 0.5λ plate in the centre of a λ by λ, whereby the rest of the plate is made up of a grid. The next step was to reverse the GTD and MOM, by placing the grid on the inside of the plate and the GTD plate on the outer edges. The third iteration has been run as in the first iteration, but the inside plate has been enlarged to 0.8 by 0.8λ A fourth simulation was run to confirm the conclusions made from the previous iteration and consisted firstly of a 1λ by 1λ and then a 1.6λ by 1.6λ plate, inside a grid 2λ by 2λ.

The reason for attempting the interaction between MOM and GTD on a plate is to gain some feedback on whether it is possible to use GTD on the less important areas and MOM on the more detailed sections. The interaction matrix will allow the user to reduce the permutations on larger structures, which require large amount of segments, and therefore computer power.

Figure 1 shows the construction of the plate, combining MOM and GTD. Figure 1 a shows the plate gridded using MOM on the outside and GTD solid plate on the inside. Figure 1 b is the inverse with the GTD plate being on the edges and the grid in the centre.

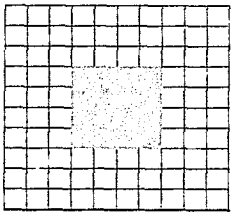


Figure 1 (a)

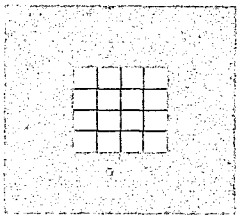


Figure 1 (b)

Firstly the simulation was run with the inner half as a GTD plate and the outer section made of a MOM grid. The results gave no real comparison to the simple GTD or simple MOM plate and dipole, no matter which reflections and diffraction terms were turned on or off.

Figure 2 shows the radiation patterns generated in SNEC for the Plate and 600MHz dipole, as shown in figure 1a.

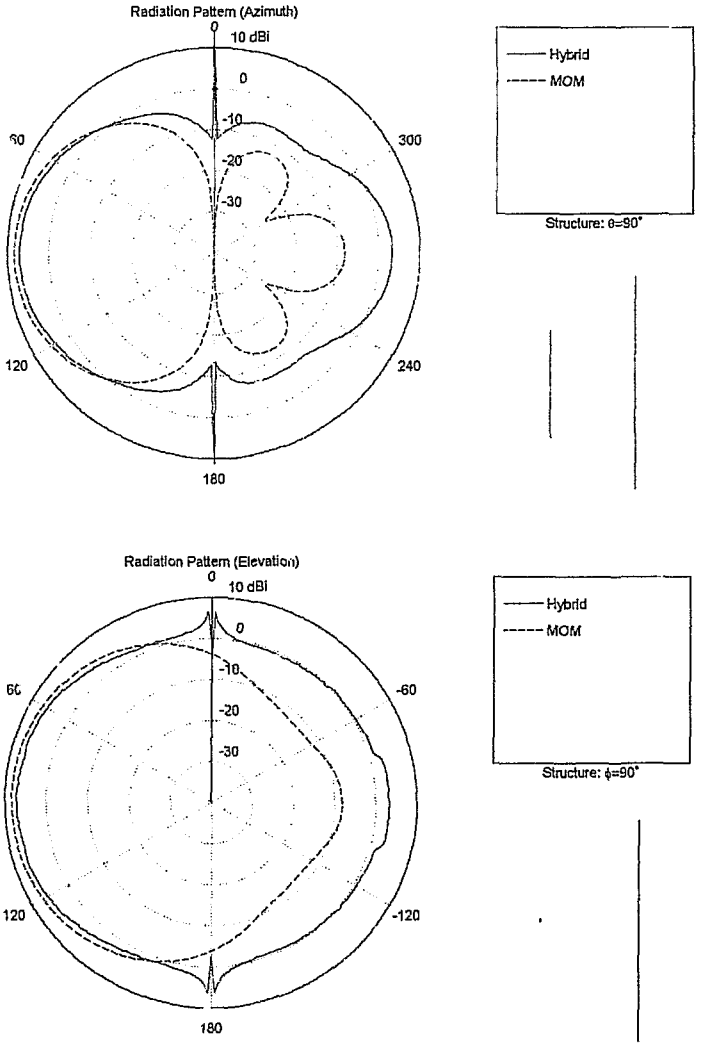


Figure 2: Elevation and azimuth plots with a 0.5λ by 0.5λ GTD plate in the centre and a MOM grid making up the rest of the λ by λ plate. Solid line (---) is the hybrid and the dotted line (- - -) is the complete MOM plate.

Better results were obtained by swapping the GTD plate and the MOM grid areas around, i.e. the grid in the centre and the plate on the outer

edge. Once again, turning on and off various reflection and diffraction terms made the results no better than the default simulation.
The better results may be due to the plate having a larger length, which has at least one side equal to a wavelength long. The patterns are still not good enough to do any design work from as can be seen in figure 3 which shows the radiation patterns. Figure 3 shows the pattern with reflection from the internal edges turned off (CR=0). Figure 4 shows the pattern with reflection from all edges, including internal edges turned on (CR=1), 5 with all diffraction and triple diffraction and reflections turned off (FC=0), and 6 with every diffraction and reflection turned on (all FC=1).

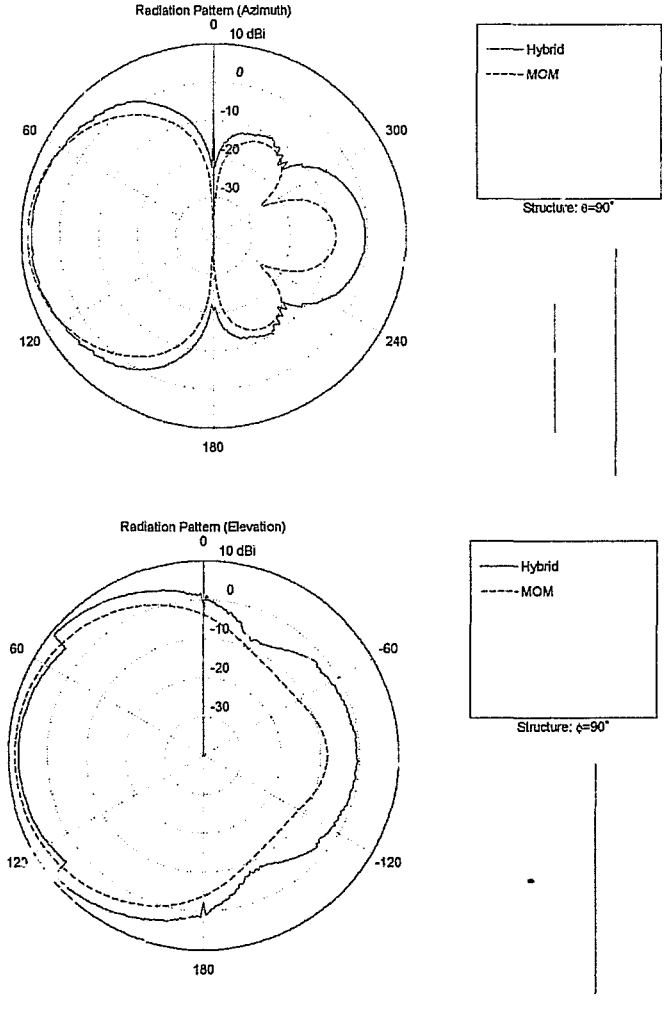


Figure 3: Elevation and azimuth plots with a 0.5λ by 0.5λ MOM grid in the centre and a GTD plate making up the rest of the λ by λ plate. CR=0 FC= default. Solid line (---) is the hybrid and the dotted line (- - -) is the complete MOM plate.

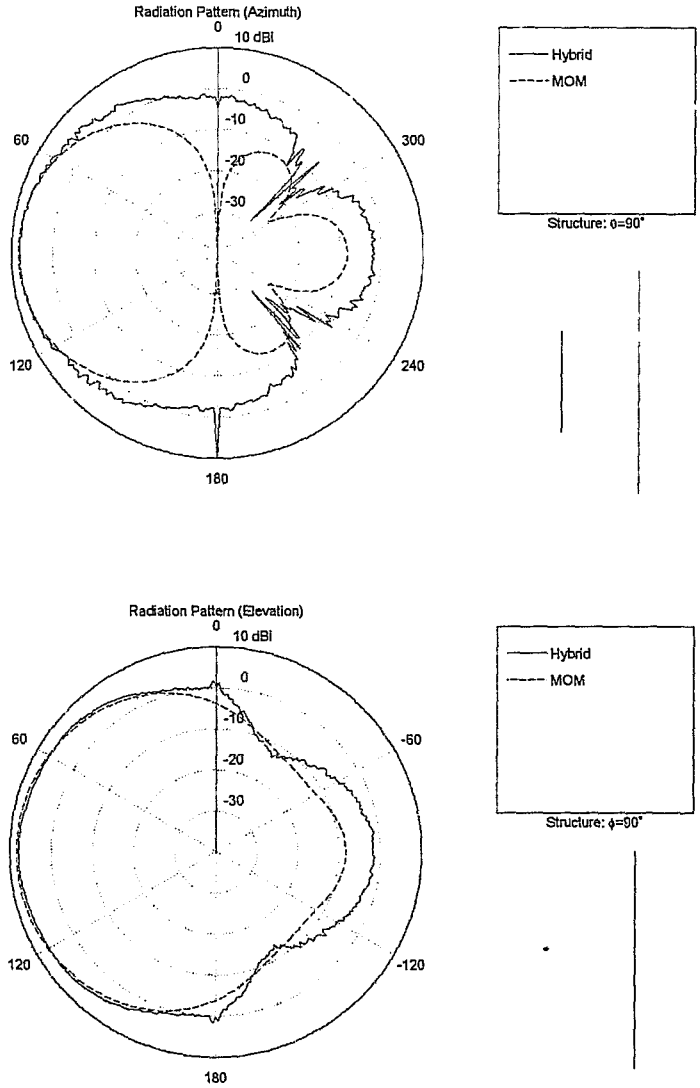


Figure 4: Elevation and azimuth plots with a 0.5λ by 0.5λ MOM grid in the centre and a GTD plate making up the rest of the λ by λ plate. CR=1 FC= default. Solid line (---) is the hybrid and the dotted line (- - -) is the complete MOM plate.

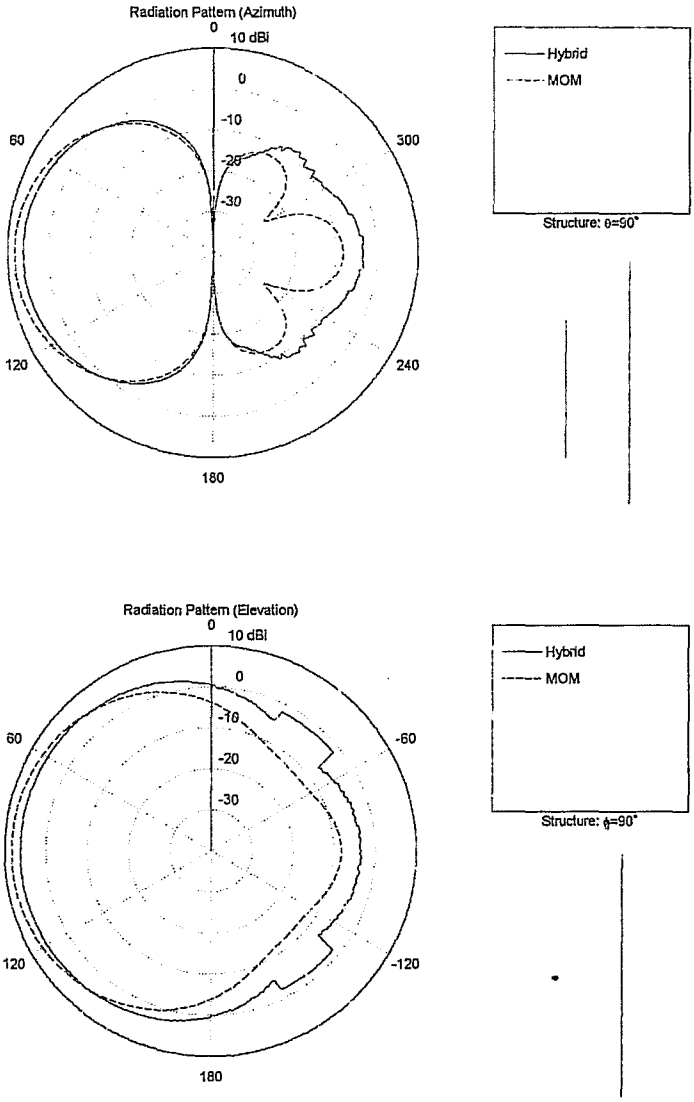


Figure 5: Elevation and azimuth plots with a 0.5λ by 0.5λ MOM grid in the centre and a GTD plate making up the rest of the λ by λ plate. CR=0; all FC= 0. Solid line (---) is the hybrid and the dotted line (- - -) is the complete MOM plate.

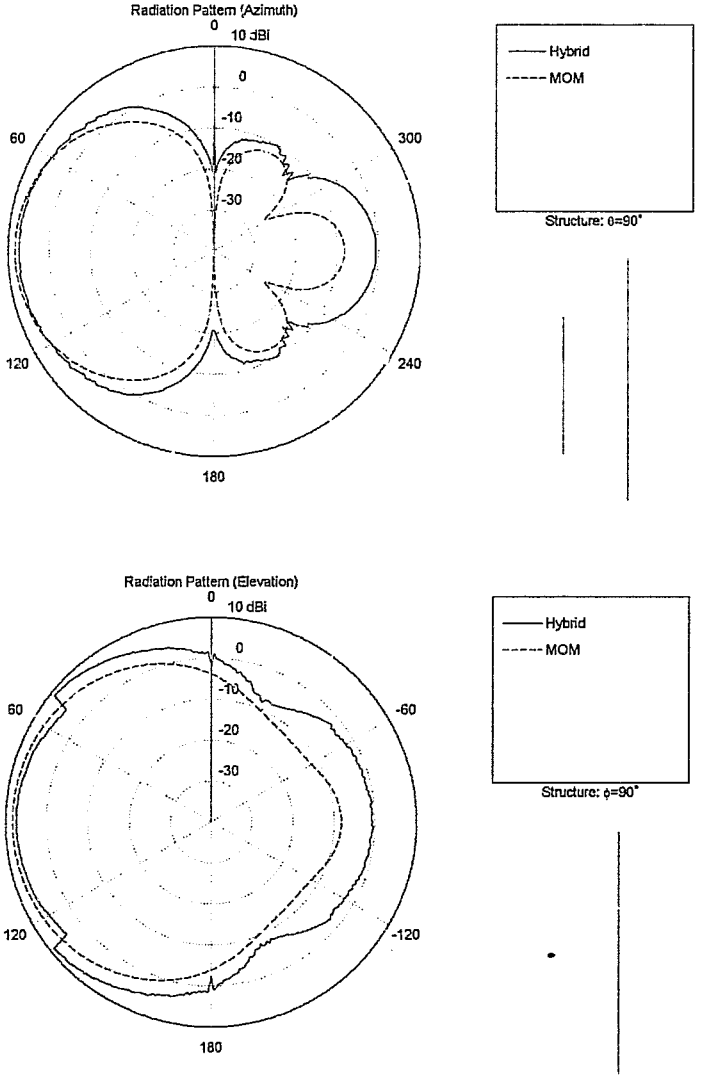


Figure 6: Elevation and azimuth plots with a 0.5λ by 0.5λ MOM grid in the centre and a GTD plate making up the rest of the λ by λ plate. CR=0; all FC= 1. Solid line (---) is the hybrid and the dotted line (- - -) is the complete MOM plate.

The third simulation was run as in figure 1a, except that the internal GTD plate area has been increased to 0.8λ by 0.8λ and the MOM grid making up the rest of the 1λ by 1λ area. The fourth simulation follows the third simulation but with a larger plate (1λ by 1λ) and a 3λ grid on the outside.

Results are much improved, from the first two simulations, confirming that the normal GTD rules still hold in SNEC, in that the lengths of the edges must be not be smaller than a wavelength in order for accurate measurements to be obtained [Lo 93].
Figure 7 shows the radiation pattern for the 0.8 by 0.8λ plate on the inside and the MOM grid on the outer edge of the λ by λ plate. The simulation has been run using the default settings for reflection and diffraction terms.

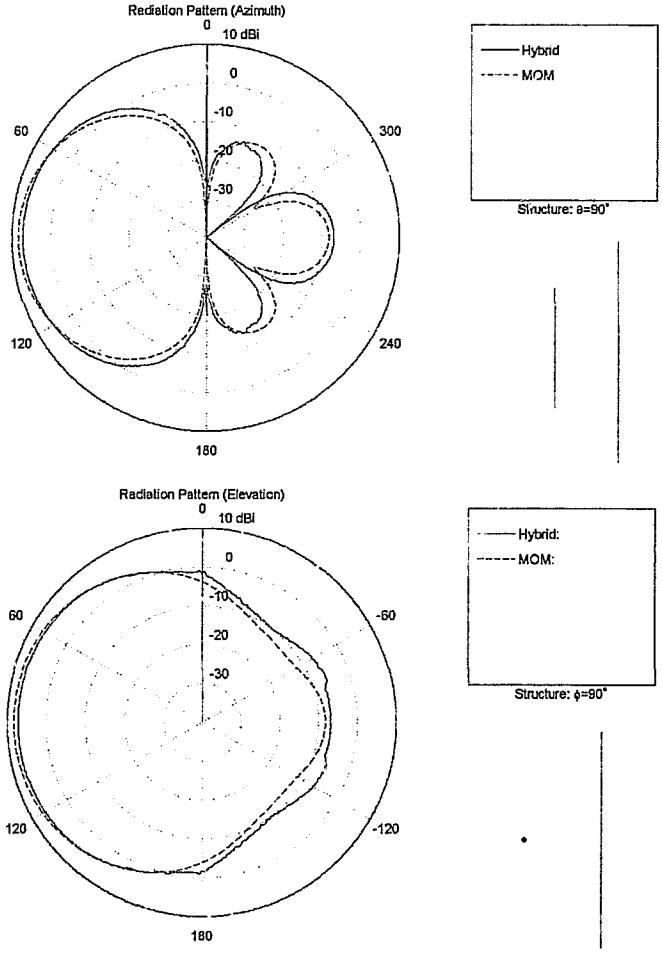


Figure 7: Elevation and azimuth plots with a 0.8λ by 0.8λ GTD plate in the centre and a MOM grid making up the rest of the λ by λ plate. CR=1; FC= default. Solid line (---) is the hybrid and the dotted line (- - -) is the complete MOM plate.

Figure 8 shows the radiation pattern for the 2λ by 2λ reflector plate with a 1λ UTD plate covering 50% of the 2λ area and with a 1.6λ plate covering 80% of the 2λ area. The simulation has been run using the default settings for reflection and diffraction terms.

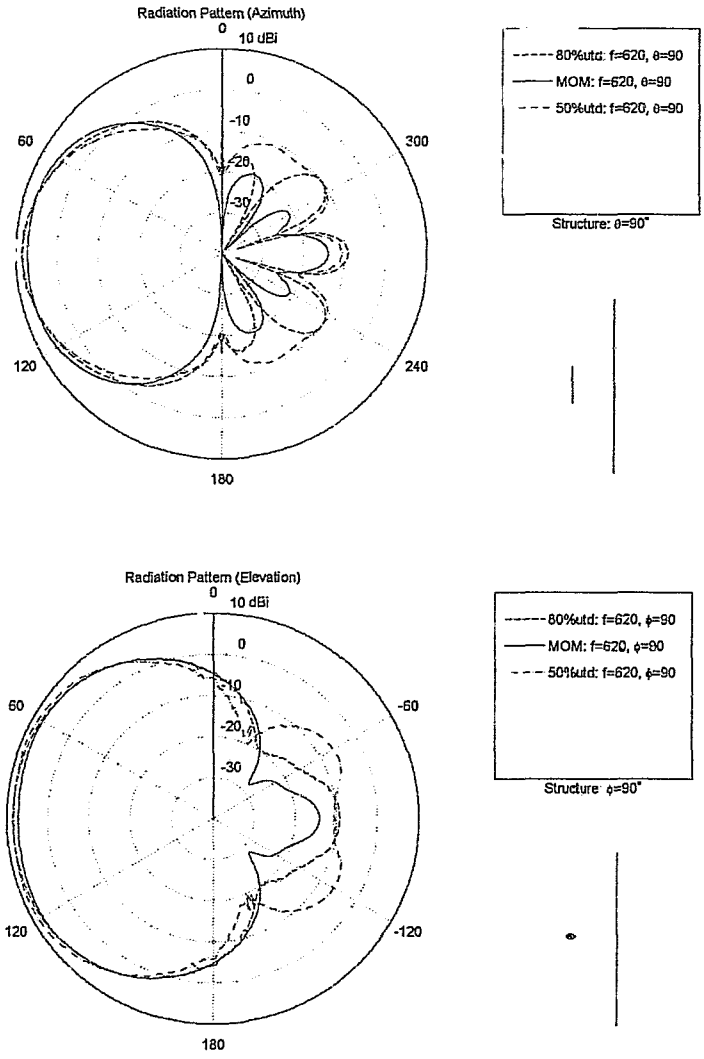


Figure 8: Elevation and azimuth plots with a 1λ by 1λ GTD plate in the centre and a MOM grid making up the rest of the 3λ by 3λ plate. CR=1; FC= default. Solid line (---) is the hybrid and the dotted line (- - -) is the complete MOM plate.

2 Conclusion

The usual GTD rules still hold in SuperNEC in that the GTD plate must have lengths that are equal to or are larger than λ in order for usable results to be obtained.

The simulations also prove that an interaction matrix, using both GTD and MOM on joining structures, is possible, provided that the GTD structure is large enough. The interaction matrix will allow users to reduce the complexity of larger structures by using this type of interaction matrix. The smaller more detailed areas can then be simulated using a wire grid and MOM.

3 References

Lo Y.T., Lee S.W. 'Antenna handbook vol1' 1993 Pathak chapter 4 'Techniques for high frequency problems'

Author Rebuli, Craig Dino
Name of thesis SuperNEC Method of Moments and Geometric Theory Diffraction Hybrid evaluation / Craig Dino Rebuli. 1999

PUBLISHER:
University of the Witwatersrand, Johannesburg
©2013

LEGAL NOTICES:

Copyright Notice: All materials on the University of the Witwatersrand, Johannesburg Library website are protected by South African copyright law and may not be distributed, transmitted, displayed, or otherwise published in any format, without the prior written permission of the copyright owner.

Disclaimer and Terms of Use: Provided that you maintain all copyright and other notices contained therein, you may download material (one machine readable copy and one print copy per page) for your personal and/or educational non-commercial use only.

The University of the Witwatersrand, Johannesburg, is not responsible for any errors or omissions and excludes any and all liability for any errors in or omissions from the information on the Library website.